Numerical study of conjugate mass transfer from a spherical droplet at moderate Reynolds number

Azeddine Rachih [a,b], Dominique Legendre [b], Eric Climent [b], Sophie Charton [a,*]

[a] CEA,DES, ISEC, DMRC, Univ. Montpellier, Marcoule, France
[b] Institut de Mécanique des Fluides de Toulouse (IMFT), Université de Toulouse, CNRS, Univ. Paul Sabatier, Toulouse INP, Toulouse 31400, France

ARTICLE INFO

ABSTRACT

Hydrodynamics and conjugate mass transfer from a spherical droplet at low to moderate Reynolds number have been investigated by direct numerical simulation. The study particularly focuses on the coupling between the internal and external flows, and their respective effects on the resulting mass transfer of a solute under 2D axi-symmetric configuration. The influence of the viscosity, density, and diffusivity ratios (μ^*, ρ^* and D^* respectively) between the two phases, as well as that of the equilibrium constant k (or Henry's number) characterizing thermodynamic equilibrium at the interface, has been studied in a range of flow Reynolds numbers relevant for solvent extraction processes (up to Reynolds number 100).

The temporal evolution of the Sherwood number has been analyzed and a general correlation is proposed for its steady state regime. Interestingly, simulation results show that correlations available in the literature in the limiting cases $k\sqrt{D^*} \ll 1$ and $k\sqrt{D^*} \gg 1$, referred to as *internal* and *external* mass transfer regimes, are not always appropriate in the context of conjugate mass transfer. This limits the use of the addition rule of transfer resistances, which reflects the flux continuity in the double stagnant film model. Indeed, a significant discrepancy is observed under specific configurations, especially at low Péclet number ($Pe \leq 500$) where non uniform interface concentration prevails.

1. Introduction

Mass transfer to/from a translating drop in an immiscible and quiescent liquid has been widely investigated, both experimentally and numerically for liquid-liquid mixtures typically encountered in solvent extraction processes [1]. It is intrinsically a complex and multi-variable problem, as under most operating conditions, depending on their size and relative velocity, droplets can be seen either as rigid objects, where diffusion is the only internal transport mechanism, or with internal circulation, where both diffusion and advection contribute to the inner mass transfer process [2,3]. Coupling between mass transfer and hydrodynamics is making the physics sensitive to many dimensionless numbers such as viscosity, mass diffusivity and density ratios.

The first comprehensive study of droplet hydrodynamics is the seminal book by Clift et al. [4], where the shape of drops is particularly discussed, depending on the respective values of the Reynolds, Eötvos (or Bond) and Morton numbers. A droplet remains spherical as long as both the Bond and Weber number are smaller than unity. Considering for example a liquid-liquid system with a difference of density of order $200\,\text{kg/m}^3$, densities of order $10^3\,\text{kg/m}^3$, dynamic viscosities of order 10^{-3} Pa s and a surface tension of order $0.02\,\text{N/m}$, the Bond number condition $Bo < 1$ yields droplet diameter smaller than 3 mm while the condition on the Weber number (based on the terminal velocity) $We < 1$ corresponds to droplet diameter smaller than 2 mm. Thus, for common liquid-liquid system the sphericity condition is satisfied for droplets smaller than 2 mm.

Regarding the mass transfer problem, as for heat transfer, three regimes are usually distinguished depending on the location of the strongest mass transfer resistance. These regimes are generally referred to as: (i) internal problem, when the dominant resistance is located in the particle, (ii) external problem, when the strongest resistance is located outside, and (iii) conjugate problem, when both resistances are of similar order of magnitude. The major difference between heat and mass transfer resides in the interface conditions. Indeed, while in thermal problem the two sides of the interface share the same temperature, a discontinuity of the concentration of the transferred species generally prevails across the interface, which value, in a non reactive system, is fixed by thermodynamic equilibrium. Given the concentration ratio at interface under equilibrium, k, also known as the Henry's coefficient, and

Nomenclature

C_D	drag coefficient
C_D^{bubble}	drag coefficient of a bubble
$C_D^{particle}$	drag coefficient of a solid particle
C	mass concentration of the solute specie
C_0^e	initial concentration in the external fluid
C_0^i	initial droplet concentration
C_∞^e	free-stream concentration (far from drop)
$\overline{C^i}$	volume average concentration in the drop
$\overline{C_S^i}$	surface average concentration on the inner side of the interface
$\overline{C_S^e}$	surface average concentration on the outer side of the interface
D^e	diffusion coefficient in the external fluid
D^i	diffusion coefficient in the internal fluid
$D^* = \dfrac{D^i}{D^e}$	diffusivity ratio
$Fo = \dfrac{D^e t}{R^2}$	external Fourier number
$Fo^i = \dfrac{D^i t}{R^2}$	internal Fourier number
$\mathbf{F_D}$	drag force
h^i	internal mass transfer coefficient
h^e	external mass transfer coefficient
h^{INT}	mass transfer coefficient of the internal problem
h^{EXT}	mass transfer coefficient of the external problem
$\mathbf{I}$	identity tensor
$k = \dfrac{C_S^i}{C_S^e}$	equilibrium (Henry) coefficient
$Pe = \dfrac{2RU_0}{D^e}$	external Péclet number
$Pe^i = \dfrac{2RU_0}{D^i}$	internal Péclet number
Pe^i_{eff}	internal effective Péclet number
p	pressure
R	radius of the spherical droplet
r	radial coordinate
$Re = \dfrac{2\rho^e U_0 R}{\mu^e}$	external Reynolds number
Sh	global Sherwood number of the conjugate problem
Sh^e	external Sherwood number
Sh^i	internal Sherwood number
Sh^{EXT}	Sherwood number of an external problem
Sh^{INT}	Sherwood number of an internal problem
Sh_θ	local Sherwood number at angular position θ
Sh_∞	steady-state global Sherwood number
t	time
U_0	free-stream velocity
$\mathbf{u}$	velocity field
μ^e	kinematic viscosity of the external fluid
μ^i	kinematic viscosity of the internal fluid
$\mu^* = \dfrac{\mu^i}{\mu^e}$	viscosity ratio
ρ^e	density of the external fluid
ρ^i	density of the internal fluid
$\rho^* = \dfrac{\rho^i}{\rho^e}$	density ratio
$\boldsymbol{\tau}$	viscous stress tensor
θ	angular coordinate (taken from the front of the droplet)

$D^* = D^i/D^e$ the solute diffusivity ratio, the asymptotic behaviour of the mass transfer regime can be assessed by the value of the dimensionless quantity $k\sqrt{D^*}$ [5].

For internal problems ($k\sqrt{D^*} \ll 1$), the interface concentration C_s is fixed by the external flow, and is supposed constant and uniform. An analytic solution was proposed by Newman [6] in the simplified case of pure diffusion in a spherical droplet. The author has shown that an asymptotic value of the Sherwood number, here noted as $Sh^{INT} = h^{INT}R/D^i$, is reached corresponding to $Sh_{Newman} = 6.58$. Later, Kronig and Brink [7] considered the case of a circulating droplet in a creeping flow ($Re \ll 1$). They highlighted a significant increase in the mass transfer rate due to the internal flow circulation obtaining a distinct asymptotic value for the internal Sherwood number $Sh^{INT} = Sh_{Kronig} = 17.9$. Except from these simplified configurations, the derivation of an analytic solution is not straightforward, and a numerical approach is required. Still assuming creeping flow, Juncu [2], Wylock et al. [5], Brignell [8] solved the mass transfer equation assuming droplet hydrodynamics is following the Hadamard-Rybczynski analytic solution. More recently, Colombet et al. [9] considered the effect of higher Reynolds number flows ($0.1 \leq Re \leq 100$) thanks to numerical simulations of both the Navier-Stokes and mass transfer equations. The study was however restricted to the case of bubbles, i.e. with small viscosity ratio ($\mu^* = 0.018$) and concentration continuity at the interface ($k = 1$).

In the case of an external problem ($k\sqrt{D^*} \gg 1$), the resolution is generally easier, since uniform concentration prevails both within the droplet and at the interface. Thus, most of the reported studies consider a steady and uniform concentration (or temperature) at the interface. In their seminal work, Feng and Michaelides [10] have studied numerically the effect of the particle viscosity on mass transfer at low Re, Abramzon and Fishbein [11] addressed numerically the solution of the convection-diffusion equation case in a creeping flow, from moderate to high Péclet numbers $1 < Pe < 10000$ [12]. Since then, many correlations were proposed for the Sherwood number of the external problem, here referred to as Sh^{EXT}, for intermediate Reynolds, and focusing e.g. on the effects of density [13] and viscosity [14] ratios or surface contamination [15]. Considering gas dissolution problems, the effect of surface active chemical species [16], or bubble shape (in term of aspect ratio) and shape transition [17] on the liquid-side mass transfer coefficient have been studied experimentally. In both studies, rising single CO_2 bubbles were monitored in time thanks to a high speed camera and proper image processing is used to measure their volume providing information on mass transfer.

While the internal and external problems have been extensively studied, conjugate interfacial transfer is still an open area for research. Indeed, tackling the conjugate problem involves taking into account the concentration in both the continuous and the dispersed phases. As mentioned previously, one particularity is that the interfacial concentration is ruled by both thermodynamic equilibrium (Henry's law) and the continuity of mass flux. Reported studies and correlations are hence restricted to particular conditions for which hydrodynamics can be simplified. A review of the main empirical correlations relevant for solvent extraction applications was proposed by Kumar and Hartland [18]. A first analytic solution for the Sherwood number was derived by Ruckenstein [19] under creeping flow assumption, using similarity variables to simplify the set of equations. Regarding numerical studies, Oliver and Chung [20] solved the transient diffusive convective heat balance equation in a flow field governed by the Hadamard-Rybczynski flow. They studied the effect of the heat capacity ratio for different Péclet numbers. Kleinman and Reed [21] performed similar study in the case of mass transfer, including the influence of k in their parametric study. They were the first to report an in-

consistency in the use of the asymptotic values, *i.e.* Sh^{INT} and Sh^{EXT}, respectively relative to the simplified internal and external problems, to estimate the global Sh of the conjugate problem from the resistances addition rule. Based on CFD simulations on a 2D axisymmetric domain, Paschedag et al. [22], carried out a more general parametric study of the temporal evolution of the Sherwood number. However, while the authors investigated the effects of *Re, Pe* and μ^*, they did not consider the influence of solute thermodynamic equilibrium between the two phases, which makes their study equivalent to conjugate heat transfer one ($k = 1$).

In the present work, a study of conjugate mass transfer based on direct numerical simulations (DNS) is reported. DNS permits to achieve a comprehensive parametric analysis, without any restriction regarding the flow and mass transfer regimes (*Re, Pe*), the fluid system (μ^*, ρ^*, D^*), and the equilibrium conditions ($k \neq 1$) which is much more complicate by experiments (regarding *e.g.* initial conditions, pollutants and surface contamination). Numerical experiments also provide access to all time and local variables, which is very valuable for understanding. The paper is organized as follows. The numerical approach and resolution procedure are described in Section 2 where the governing equations, mesh, and typical conditions implemented at the interface are successively introduced. Section 3 is dedicated to the preliminary validations. In this aim, relevant references from the literature are considered to assess the performances of the developed model in terms of drag coefficient C_D, and Sherwood number Sh. Finally, a detailed parametric study of the conjugate mass transfer problem is commented in Section 4.

2. Numerical model

2.1. Governing equations

A spherical, non-deformable, and non contaminated droplet is considered. Both internal and external fluids are assumed Newtonian, and with constant and uniform physical properties (density, viscosity) in each phase. The transferred solute undergoes no chemical reaction. The problem is assumed to be axi-symmetric. The resulting 2D domain is divided into two distinct sub-domains: one referring to the droplet inner phase ($\delta = i$) and the second one corresponding to the continuous outer phase ($\delta = e$).

The unsteady Navier-Stokes and mass balance equations Eqs. (1)–(3), are considered in both phases:

$$\nabla \cdot \mathbf{u}^\delta = 0 \tag{1}$$

$$\rho^\delta \left(\frac{\partial \mathbf{u}^\delta}{\partial t} + \nabla(\mathbf{u}^\delta \mathbf{u}^\delta) \right) = \nabla \cdot (-p^\delta \mathbf{I} + \boldsymbol{\tau}^\delta) \tag{2}$$

$$\frac{\partial C^\delta}{\partial t} + \nabla \cdot (C^\delta \mathbf{u}^\delta) = D^\delta \nabla^2 C^\delta \tag{3}$$

where ρ^δ is the fluid density, $\mathbf{u}^\delta$ the velocity field, p^δ is the pressure, $\boldsymbol{\tau}^\delta$ the viscous stress tensor, C^δ the transferred specie concentration, and D^δ its diffusion coefficient in the considered phase δ. $\mathbf{I}$ the identity tensor. Balance equations are solved in a dimensionless frame, using the drop radius R as the reference length, and the free stream velocity U_0 as the velocity scale. The discretized equations are provided in Appendix A.1.

2.2. Mesh and discretization

An orthogonal curvilinear coordinates system (ξ_1, ξ_2) is used, as proposed by Magnaudet et al. [23]. It is depicted in Fig. 1. It consists in two adjacent domains, one of them (the droplet, phase i) is discretized using a polar mesh centred at the droplet center, while the other (the external phase, e) is based on the equipotentials and streamlines of an inviscid fluid flow around a cylinder.
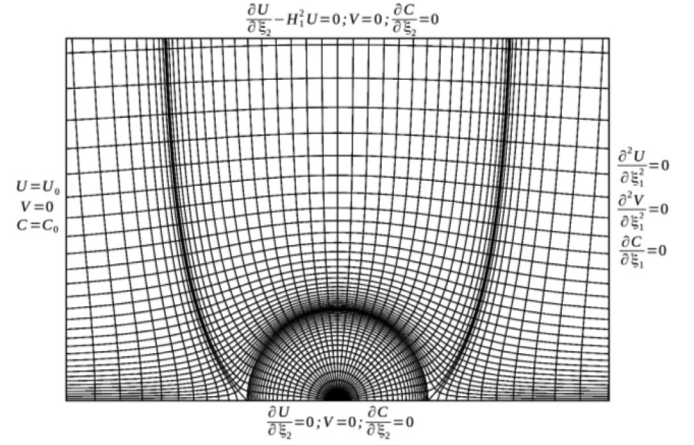

Fig. 1. 2D mesh and boundary conditions (see notations in Appendix A.2). The bottom boundary corresponds to symmetry axis $\mathbf{e}_x$ of the problem.

This mesh is then used for 2D axi-symmetric simulations around a spherical droplet. In order to ensure constant and uniform far-field conditions, the global size of the computational domain was set to approximately 50*R*.

The mesh is refined at the interface in order to ensure that at least 4 grid cells are enclosed in both the hydrodynamic and the mass transfer boundary layers, approximating the thickness of these boundary layers by $R/Re^{1/2}$ and $R/Pe^{1/2}$ respectively (where *Re* and *Pe* refer to the external phase).

The dimensionless Navier-Stokes and solute transport equations are solved in a finite volume discrete form, on a staggered mesh. The pressure nodes are located at the center of the cell while curvilinear velocities are located on the faces of each control volume.

2.3. Interface boundary conditions

The tangential velocity and shear stress are continuous at the interface while the velocity normal component is equal to 0 (solute is very dilute). Moreover, since no deformation of the spherical droplet occurs, no condition is needed for the normal stress at the interface. Therefore, the hydrodynamic jump conditions at the interface are expressed as follows, where ($\mathbf{n}$, $\mathbf{t}$) are the normal and tangential vectors to the interface, respectively:

$$\begin{aligned} \mathbf{u}_S^i \cdot \mathbf{t} &= \mathbf{u}_S^e \cdot \mathbf{t} \\ \mathbf{u}_S^i \cdot \mathbf{n} &= \mathbf{u}_S^e \cdot \mathbf{n} = 0 \\ (\boldsymbol{\tau}_S^i \cdot \mathbf{n}) \cdot \mathbf{t} &= (\boldsymbol{\tau}_S^e \cdot \mathbf{n}) \cdot \mathbf{t} \end{aligned} \tag{4}$$

where the subscript S denotes quantities evaluated at the interface. Physical properties are constant (not depending on solute local concentration) which yields that Marangoni effect is neglected.

On the other hand, the mass flux of the transferred specie is continuous (no accumulation) and thermodynamic equilibrium is assumed to prevail at the interface. This results in the following equations for the interface concentration and the concentration gradients normal to the interface:

$$\begin{aligned} C_S^i \Big| &= k C_S^e \\ D^i \frac{\partial C^i}{\partial r} \bigg|_{R^-} &= D^e \frac{\partial C^e}{\partial r} \bigg|_{R^+} \end{aligned} \tag{5}$$

where k is the dimensionless Henry coefficient. Since the computational domain consists in two coupled fluid domains, the interface conditions Eqs. (4) and (5) are implemented as coupled boundary conditions at the joint interface between the two domains. The expressions of the discretized interface conditions are given in Appendix A.1. The ability of the implemented jump conditions to

handle the concentration jump at the interface has been verified in the case of 1D diffusion problems, for hich an analytic solution exists (see Appendix A.2).

Besides the interface conditions, the following conditions are applied at the domain boundaries (Fig. 1). The external flow far from the droplet is assumed to be uniform with a velocity $U_0 \, \mathbf{e}_x$. Note that in the fixed grid domain, $U_0 \, \mathbf{e}_x$ represents the relative velocity between the droplet and the continuous phase. Constant velocity U_0 and concentration C_∞^e are imposed at the domain inlet. A symmetry condition is defined along the $\mathbf{e}_x$ axis. The top boundary is supposed to be far enough from the droplet to consider a constant velocity. Following Magnaudet et al. [23] prior work, an outflow boundary condition is defined at the downstream boundary. At last for the concentration, a Neumann condition is imposed at the top boundary, at the axis and at the outlet where the normal concentration gradient is null.

2.4. Numerical method and simulation strategy

The set of balance equations is solved using the code JADIM developed at IMFT [23–28]. The spatial discretization is based on second order-centered central difference scheme. The advective and viscous terms are calculated through a Runge-Kutta/Crank-Nicholson time advancement scheme. At the end of each time step, the divergence free condition is imposed by solving a Poisson equation on an auxiliary potential, independently inside and outside the droplet. The overall algorithm is second-order accurate both in time and space.

As we assume that the density and the viscosity of the two phases are not changing with the solute concentration, the continuity and the momentum transport equations can be solved separately from the mass transport equations. The hydrodynamic problem is solved first, for a given Reynolds number Re, viscosity ratio μ^* and density ratio ρ^*, until the steady state is reached. Then, the transient concentration equation is solved in the frozen velocity field, for a given Péclet number Pe, diffusivity ratio D^* and Henry coefficient k. As previously mentioned, the transfer is assumed to proceed from the droplet (with initial concentration $C_0^i = 1$), to the continuous phase (with initial concentration $C_0^e = 0$). The calculation is stopped when the mean dimensionless concentration falls below 10^{-5} inside the droplet.

2.5. Post-processing

The contour maps of velocity and concentration, and their gradients, are calculated at each time-step. Note that under a dimensionless framework, the governing time-scale for the transport process is expressed by the external Fourier number $Fo = D^e t / R^2$. Various mass transfer quantities can be derived from the DNS results to assess the evolution of mass transfer.

The internal and the external Sherwood number, Sh^i and Sh^e, are defined by Eqs. (6) and (7) considering the respective driving concentration differences $\Delta C^i = \overline{C^i} - \overline{C_S^i}$ and $\Delta C^e = \overline{C_S^e} - \overline{C_\infty^e}$. With these definitions, $\overline{C^i}$ stands for the volume average concentration within the spherical droplet, and $(\overline{C_S^i}, \overline{C_S^e})$ for the surface average concentrations on both sides of the interface. We remind that in virtue of the thermodynamic equilibrium, these latter verify the Henry's relation $\overline{C_S^i} = k \overline{C_S^e}$.

$$Sh^i = \frac{-\int_S \frac{\partial C^i}{\partial r}\Big|_{r=R-} dS}{4\pi R \left(\overline{C^i} - \overline{C_S^i}\right)} \tag{6}$$
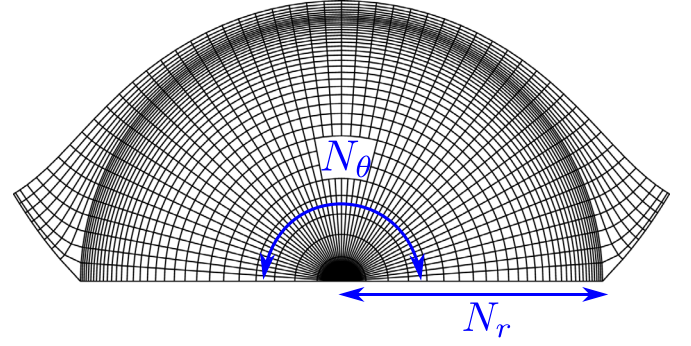

Fig. 2. Radial and angular parameters of mesh refinement.

Table 1
Effect of mesh refinement on Sh for various Pe ($\mu^* = 1$, $D^* = 1$, and $Re = 100$).

Pe	Mesh $N_r \times N_\theta$			
	50×80	60×100	70×100	100×120
10	1.742	1.745	1.745	1.746
100	5.501	5.505	5.507	5.507
1000	12.404	12.413	12.399	12.385
10000	16.911	16.903	16.9	16.87

$$Sh^e = \frac{-\int_S \frac{\partial C^e}{\partial r}\Big|_{r=R+} dS}{4\pi R \left(\overline{C_S^e} - C_\infty^e\right)} \tag{7}$$

where the average concentrations are obtained according to:

$$\overline{C_S^i} = \frac{1}{2} \int_0^\pi C_S^i(\theta, t) \sin(\theta) d\theta \tag{8}$$

$$\overline{C_S^e} = \frac{1}{2} \int_0^\pi C_S^e(\theta, t) \sin(\theta) d\theta \tag{9}$$

$$\overline{C^i} = \frac{3}{2R^3} \int_0^R \int_0^\pi C^i(r, \theta, t) r^2 \sin(\theta) dr d\theta \tag{10}$$

where r and θ are the radial coordinate and polar angle used to parameterize the drop volume. The global Sherwood number is defined considering as driving force the difference between the instantaneous droplet average concentration, $\overline{C^i}$, and the free stream concentration C_∞^e:

$$Sh = \frac{-R}{2\left(\overline{C^i} - C_\infty^e\right)} \int_0^\pi \frac{\partial C^i}{\partial r}\Big|_{R-} \sin(\theta) d\theta \tag{11}$$

At last, the local Sherwood number, i.e. at a particular angular position θ along the interface, can also be deduced from the simulation results. It is defined by:

$$Sh_\theta = \frac{-R}{\left(\overline{C^i} - \overline{C_S^i}\right)} \frac{\partial C^i}{\partial r}\Big|_{R-} \tag{12}$$

2.6. Mesh convergence analysis

Particular care was taken to properly set the radial and angular mesh refinement around the droplet (see Fig. 2). The same expansion ratio was considered on each side of the interface in order to guarantee a smooth transition from the inside to the external region of the drop. Due to the specific structure of the external mesh, refining angular mesh yields refining the outer region just outside the droplet. Mesh sensitivity of the steady-state values of the Sherwood number is reported in Table 1. For low Péclet number,
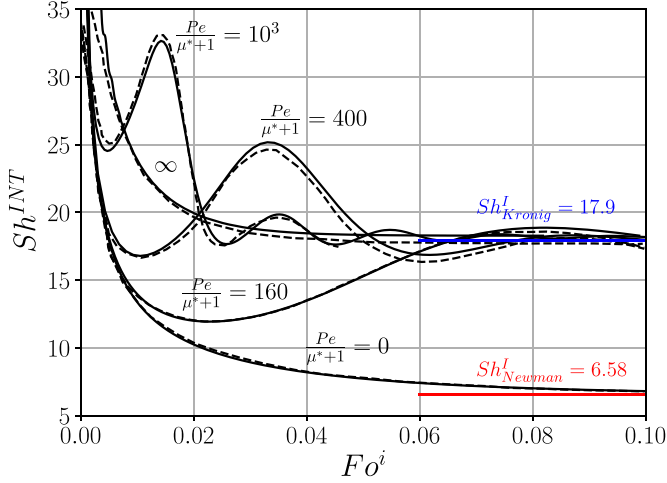
Fig. 3. Time evolution of the Sherwood number Sh^{INT} for different values of $Pe/(\mu^* + 1)$. The solid line represents the DNS results, and dashed lines those from Clift et al. [4].

Fig. 4. Angular profiles of the local Sherwood number for different Fourier numbers. Comparison between our DNS results (in black) and [30] (in blue) ($Pe = 1000$, $\rho^* = 1$, $\mu^* = 1$, $D^* = 1$). (For interpretation of the references to colour in this figure legend, the reader is referred to the web version of this article.)

Table 2
Steady-state Sherwood number Sh_∞ for conjugate mass transfer at low Reynolds ($Re = 0.1$) and ($\mu^* = 1$). Comparison between our DNS results and data from Oliver and Chung [20].

Pe	50	100	200	500	1000
Present simulations	2.72	3.6	4.8	7.19	9.14
Olivier & Chung	2.67	3.6	4.8	7.2	9.2

no significant deviation is observed over the wide range of conditions investigated highlighting that mesh convergence is achieved. At high Pe number ($Pe > 1000$), a finer mesh was required to reach convergence of numerical results due to thinner boundary layer.

3. Validation and preliminary results

Prior to the investigation on conjugate mass transfer problem at moderate Re, different case-studies from the literature were first considered in order to further validate the numerical accuracy.

3.1. Drag coefficient

The drag coefficient C_D is a global physical quantity relevant to validate hydrodynamic simulations. It is defined, with the considered notations by:

$$C_D = 2 \frac{\mathbf{F_D} \cdot \mathbf{e_x}}{\pi \rho^e U_0^2 R^2} \qquad (13)$$

where $\mathbf{F_D}$, the total drag force exerted by the uniform flow on the sphere, can be obtained from the DNS results using:
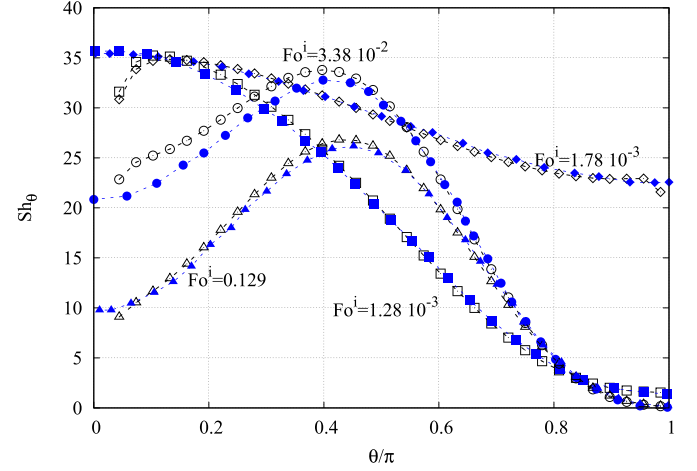
$$\mathbf{F_D} = \int_S [-p^e \mathbf{n} + (\tau_I^e \cdot \mathbf{n})]dS \qquad (14)$$

The C_D values obtained by DNS are in excellent agreement with the correlation of Feng and Michaelides [29] (Eq. (B.4) in Appendix B), with a difference of less than 1%. Thus, numerical simulations accurately predict the hydrodynamics of the particle, which is also highlighted by the analysis of the separation angle (see Appendix B.1).

3.2. Internal transfer under Stokes flow

Mass transfer simulations were achieved at low Reynolds number (i.e. $Re = 0.1$). Uniform and constant concentration was considered in the external fluid and at the droplet interface, to simulate internal transfer under Stokes flow conditions. The time evolution of the Sherwood number (Sh^{INT}) predicted by DNS is compared in Fig. 3 with the predictions from Clift et al. [4], in which the Stokes flow is prescribed by Hadamard-Rybczynski analytical solution for both external and internal velocity distributions.

The transient and steady regimes are well reproduced by our DNS results, both for the "rigid" and the "circulating" droplet cases.

- For a rigid sphere ($\frac{Pe}{\mu^*+1} \rightarrow 0$), where diffusion is dominating mass transfer, the simulation correctly predicts the monotonic decrease of the Sherwood number. The value of Sh^{INT} converges towards $Sh_{Newman} = 6.58$, in agreement with the steady value predicted by Newman [6].
- When circulation flow (Hill's vortex) takes place inside the droplet ($\frac{Pe}{\mu^*+1} \rightarrow \infty$), oscillations of mass transfer are observed, whose amplitude reduces over time, before reaching the steady value $Sh_{Kronig} = 17.9$ predicted by Kronig and Brink [7].

Moreover, our simulations accurately predict mass transfer profiles along the interface, as illustrated in Fig. 4, where the local (or angular) Sherwood number Sh_θ, Eq. (12) is compared to the numerical data provided by Juncu [30].

3.2.1. Conjugate mass transfer with moderate Reynolds number ($Re \leq 10$)

When the resistance to transfer is evenly distributed on both sides of the interface, one must solve the mass balance equations in both the internal and the external fluids with appropriate boundary conditions at the interface. Referring to Oliver and Chung [20], we considered the case of a spherical droplet, at low Reynolds number ($Re = 0.1$) and fluids with equal viscosities $\mu^* = 1$. The inlet concentration is fixed while outlet and interface concentrations are free to evolve. As summarized in Table 2, the steady values of the Sherwood number Sh_∞ predicted from the DNS results are again consistent with the literature data, in the whole range of Pe considered by the authors.

Still at low Reynolds, a parametric study was carried out, based on the work of Kleinman and Reed [21], where the main dimensionless physical properties affecting mass transfer are studied. Fig. 5 illustrates the effects of the diffusivity ratio, D^*, and of the Henry coefficient, k. The behaviour reported by the authors is well reproduced by the numerical simulations, as e.g. the accelerating effect of the inner circulation occurring at high Pe. In addition, we note that:
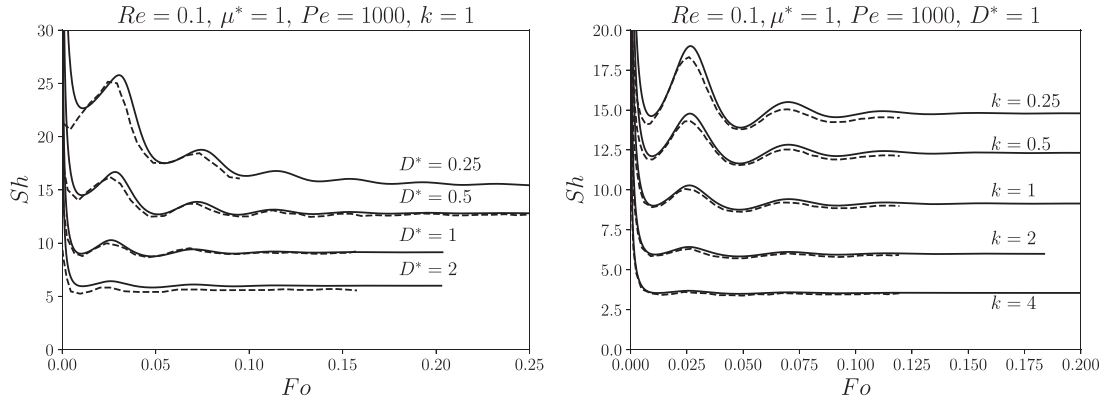
Fig. 5. Effect of D^* (left) and k (right) on the time-evolution of Sh for $Re = 0.1$ and $Pe = 1000$. The solid lines represent DNS results, and the dashed lines correspond to the results from Kleinman and Reed [21]..
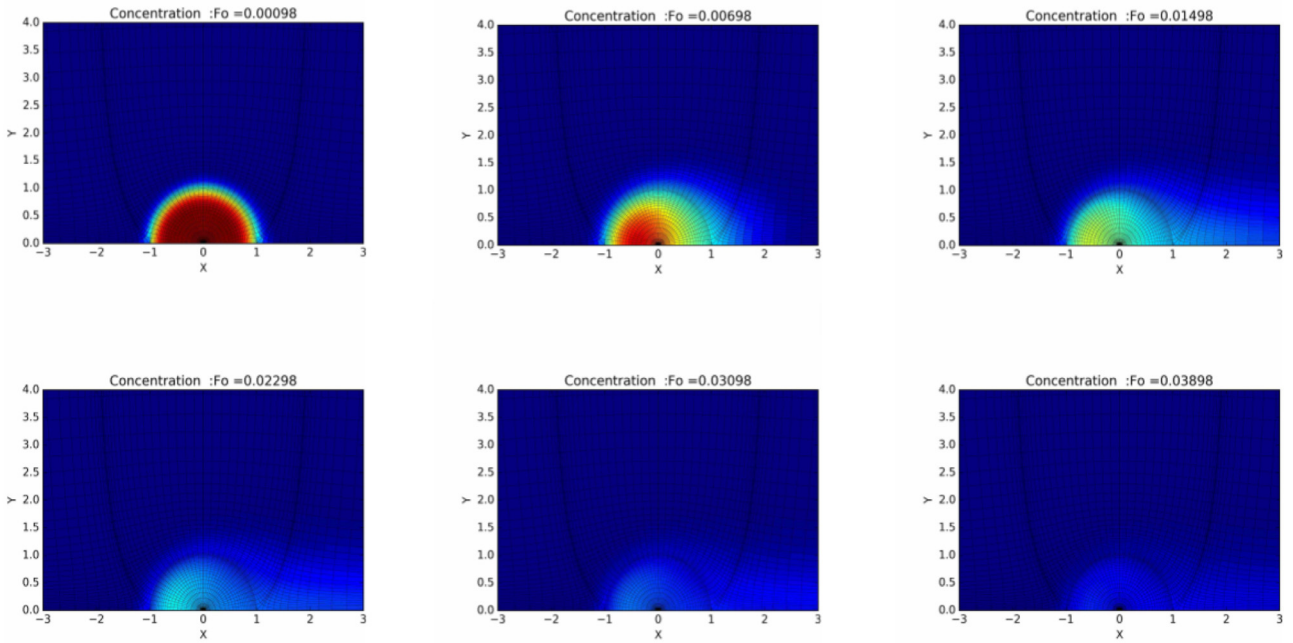
Fig. 6. Time evolution of the concentration spatial distribution for $Pe = 10$ ($Re = 10$, $\mu^* = 1$, $D^* = 1$). Colours spanning from blue to red correspond to concentration varying between 0 and 1. (For interpretation of the references to colour in this figure legend, the reader is referred to the web version of this article.)

- Increasing the value of k, which means decreasing the solute affinity for the continuous phase, results in smaller Sh, e.g. a lower mass transfer rate (right figure). It is also interesting to note that at high k values, the oscillations of Sh underlying the presence of an internal circulation are attenuated.
- Although the amplitude is reduced, no modification of the frequency of the Sh oscillations is evidenced while increasing the value of the diffusivity ratio D^* (left figure). This confirms that the Sh oscillations are due to the internal flow circulation only, and are not related to diffusion.

Interestingly, while the Sherwood value is expected to converge towards the profiles associated to the internal problem (Sh^{INT}) for low D^*, the asymptotic value predicted by the DNS for $D^* = 0.25$, ($Sh_\infty \rightarrow 15.327$) is still significantly lower than the asymptotic value predicted by Kronig and Brink [7], $Sh_{Kronig} = 17.9$.

Besides global values, DNS provides spatial distributions of the flow and concentration over the whole computational domain and at any instant. Snapshots of the solute spatial distribution in the droplet and the surrounding fluid are reported in Figs. 6 and 7 for

$Pe = 10$ and $Pe = 1000$, respectively. The effect of the internal circulation prevailing at high Pe is particularly evidenced. After some time however, the process becomes diffusion limited from a torus located in the vortex zone toward the interface. This state corresponds to the steady regime of mass transfer (plateau value of the Sherwood number).

3.2.2. Remark on the size of the computational domain

The size of the simulation domain for this study was 50R, which may seem small for simulations at small to moderate Reynolds ranging from 0.1 to 10. Indeed, simulations at very small Reynolds number require a domain size large enough to prevent confinement effect. In this study, two domain sizes 50R and 100R have been compared at $Re = 0.1$, $Sc = 1000$, $\mu^* = 1$, $D^*=1$ and $k = 1$. The difference observed was less than 1% for both for the drag coefficient and the Sherwood Number. Indeed, when the Schmidt number is larger than one, mass boundary layers are thinner than hydrodynamic ones and this limits the effect of finite extent of simulation domain on the transfer coefficient.
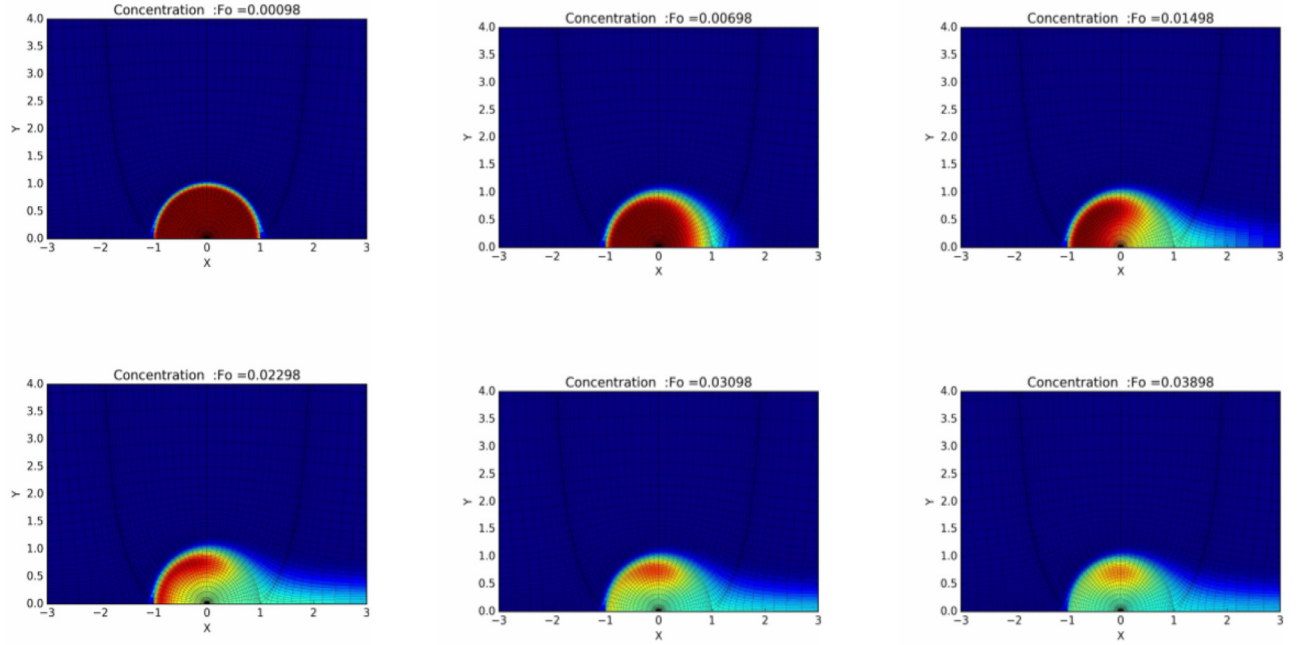
Fig. 7. Time evolution of the concentration spatial distribution for $Pe = 1000$ ($Re = 10$, $\mu^* = 1$, $D^* = 1$). Colours spanning from blue to red correspond to concentration varying between 0 and 1. (For interpretation of the references to colour in this figure legend, the reader is referred to the web version of this article.)

4. Results and discussion

4.1. Hydrodynamics and flow fields for $10 \leq \mathrm{Re} \leq 200$

A comprehensive parametric study of hydrodynamics in the range $10 \leq Re \leq 200$ was achieved. The prediction of the drag coefficient was already discussed and validated in Section 3. A full description of the flow outside and inside the moving droplet is also required for addressing the mass transfer problem, because no analytic solution exists in the range of Re investigated.

Fig. 8 illustrates some simulation results emphasizing the effect of the viscosity ratio μ^* on the flow structure, up to $Re = 150$. In

Fig. 8. Effect of Re and droplet viscosity on the flow pattern. Top: $\mu^* = 5$, bottom: $\mu^* = 100$. Left: $Re = 50$, right: $Re = 150$.

addition to the inner recirculation, already present at any Re and responsible of increased mass transfer rate compared to the rigid particle case, an external recirculation is developing in the wake of the droplet, while increasing μ^* and/or Re. The effect of this flow separation (for which additional data are reported in Appendix B.1) on mass transfer will be discussed in the next section.

The structure of the flow plays a major role on both C_D and the mass transfer rate. Hence, before attempting to correlate Sh, a first part of the study was dedicated to the evaluation of C_D correlations, in view of relating the general cases to the two asymptotic cases of the bubble ($\mu^* \to 0$, where inner circulation prevails) and the rigid particle ($\mu^* \to \infty$, where inner flow is vanishing).

In Stokes flow, Hadamard and Rybczynski derived an analytic solution for the drag coefficient around a spherical viscous droplet [4]:

$$C_D(Re, \mu^*) = \frac{8}{Re}\left(\frac{2 + 3\mu^*}{1 + \mu^*}\right) \tag{15}$$

Introducing the drag coefficient related to a solid sphere $C_D^{particle}(Re) = 24/Re$, and its corresponding value for a spherical bubble, $C_D^{bubble}(Re) = 16/Re$, both valid in Stokes flow, Eq. (15) rewrites:

$$C_D(Re, \mu^*) = \frac{C_D^{bubble} + \mu^* C_D^{particle}}{1 + \mu^*} \tag{16}$$

This expression, exact for low Reynolds numbers, indicates that regardless of the viscosity ratio, the value of C_D for a viscous drop is ranging between the bubble and the solid particle values.
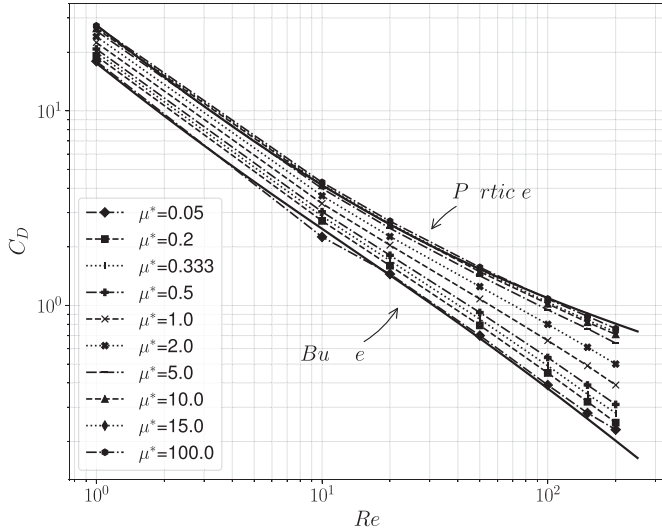
At higher Re, where no analytical solution exists, Ryvkind and Ryskin [31] proposed a correlation for the drag coefficient based on a similar decomposition (see Eq. (B.6)). They achieved quite good precision (*"sufficiently accurate for engineering calculations"*) for a viscosity ratio close to 1, and $Re \leq 100$, meaning that under these conditions also, the value typical of the droplet drag coefficient is varying between that of the bubble, and that of the solid particle.

Thanks to our numerical simulations, we evaluated the validity of Eq. (16) up to $Re = 200$ and over a much wider range of viscosity ratio, ranging from the bubble case ($\mu^* \to 0$) to the solid
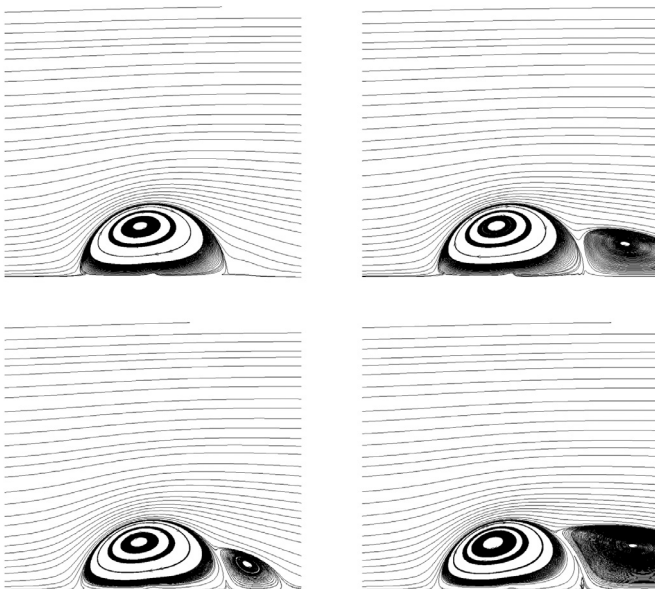
Fig. 9. Evolution of the drag coefficient with Re for bubbles, droplets and solid particles. Comparison between present simulations (symbols) and the predictions of Eq. (16) (dashed lines) using Eq. (B.8) [32] and (B.7) [33] for bubbles and particles respectively (solid lines).

Table 3
Effect of the density ratio and Reynolds number on the drag coefficient C_D.

Re / ρ^*	0.1	0.5	1	5	10
10	3.345	3.345	3.344	3.342	3.342
50	1.088	1.086	1.083	1.07	1.07
100	0.671	0.667	0.662	0.66	0.66

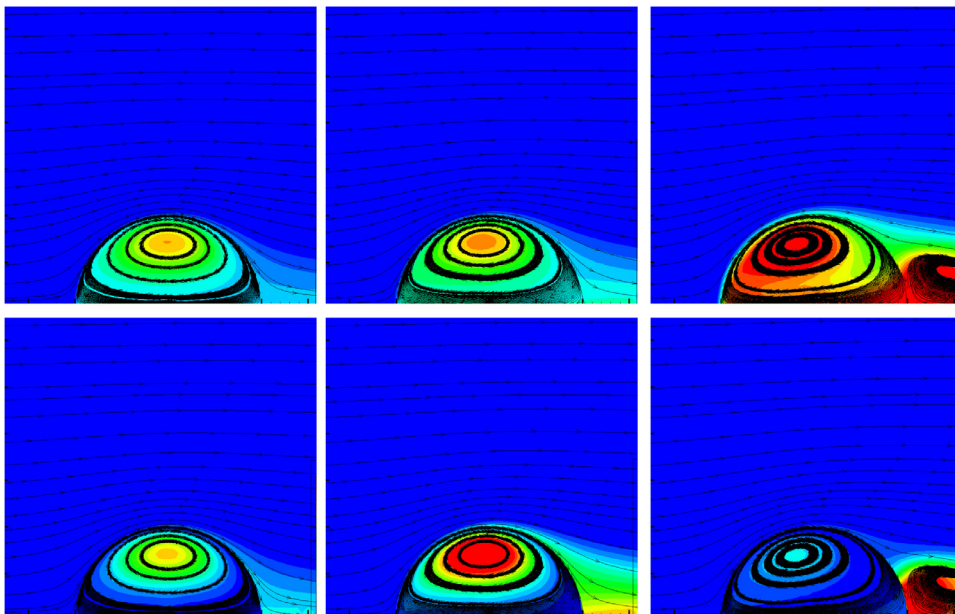### 4.2. Conjugate mass transfer up to $Re = 100$

Different mass transfer simulations were performed for each hydrodynamic configuration of Section 4.1, yielding more than 200 cases for the parametric study of the influence of Re, Pe, μ^*, D^*, and k on the internal, external, and global mass transfer resistances.

#### 4.2.1. Comments on spatial solute distribution

Examples of instantaneous solute concentrations contours in conjugate regimes are reported in Fig. 10. Those snapshots give a first overview of the effects likely to influence mass transfer in conditions typical of most engineering applications (i.e. $k \neq 1$ and $Re \gg 10$).

As previously observed in Fig. 5 for creeping flow, the effect of both internal and external flow circulations on conjugate mass transfer is weakened when the thermodynamic equilibrium is opposed to the solute transfer (case $k = 5$). Hence, the problem is controlled by the external transfer resistance, and the concentration inside the droplet is nearly uniform. Fig. 10 provides indeed a good illustration of the combined effect of μ^* and k:

- For the case $Pe = 1000$, the internal circulation plays a major role in the mass transfer process. As the viscosity ratio increases (from left to right), the intensity of circulation reduces and its center shifts towards the droplet front. The solute diffuses then slowly from the core to the interface of the droplet.
- On the other hand, while k increases (from top to bottom), the transfer resistance shifts from internal to external location. The effect of the internal circulation on the concentration spatial

particle ones ($\mu^* \to \infty$). Adequate correlations from the literature were used in this aim, respectively reported by Mei et al. [32] and Schiller and Nauman [33] for C_D^{bubble} and $C_D^{particle}$ (see Appendix B.2).

As evidenced by Fig. 9, Eq. (16) yields interestingly a very good prediction of C_D values over the whole range of viscosity ratio considered. As in Stokes flow, the drag coefficient is observed to stand between the corresponding values for the particle and the bubble. Note that while μ^* and Re are the main parameters influencing C_D, as already evidenced by Feng and Michaelides [29], the density ratio ρ^* on the other hand has a negligible effect (see Table 3).

Besides the steady drag force, the DNS model was also used to investigate the Basset-Boussinesq (or history) force experienced by the droplet [34].

Fig. 10. Superimposed concentration contours and streamlines ($Fo^i = 0.15$, $Re = 100$, $Pe = 1000$, $D^* = 1$) for different equilibrium constants (top: $k = 1$, bottom: $k = 0.1$) and viscosity ratio (from left to right: $\mu^* = 0.25, 1, 5$). Colours spanning from blue to red correspond to concentration varying between 0 and 1. (For interpretation of the references to colour in this figure legend, the reader is referred to the web version of this article.)
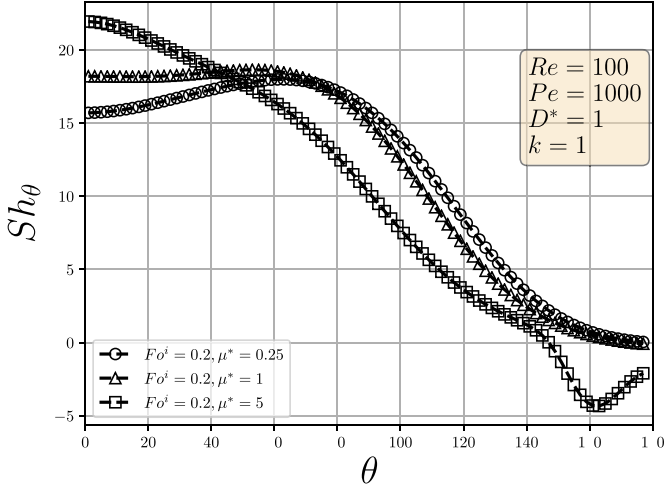
Fig. 11. Angular evolution of the local Sherwood number Sh_θ under steady regime with the viscosity ratio. Specific effect of the external wake flow prevailing at $\mu^* = 5$.

Fig. 12. Evolution of steady internal Sherwood number with internal effective Péclet number Pe^i_{eff} [14]: $Re = 100$, $\mu^* = 0.5(\square)$ $\mu^* = 1(\triangle)$ $\mu^* = 1.5(\circ)$ $\mu^* = 2(\triangleright)$ $\mu^* = 10(\triangleleft)$; *Creeping flow*, $\mu^* = 0.5(\square)$ $\mu^* = 1(\triangle)$ $\mu^* = 1.5(\circ)$ $\mu^* = 2$ $(\triangleright)$ $\mu^* = 10(\triangleleft)$[30].: *Creeping flow*, $\mu^* = 1(\blacktriangle)$; $Re = 100$, $\mu^* = 1(\blacktriangle)$. This work: $Re = 100$, $\mu^* = 0.5(\blacksquare)$ $\mu^* = 1(\blacktriangle)$ $\mu^* = 2(\blacktriangleright)$. Dashed lines: adapted correlation from [9] Eq. (C.1).

distribution decreases, and the concentration inside the droplet becomes almost uniform.

It is interesting to note that for $\mu^* = 5$, the effect of the external wake flow strongly depends on the value of k. In particular for $k = 0.1$ (top right figure), the concentration in the vicinity of the external recirculation is larger than in the core of the droplet (transfer is reversed). The external wake flow (here observed at $\mu^* = 5$, in the right column of Fig. 10) is acting as a solute reservoir, that imposes a higher concentration in the wake of the droplet, than in the rest of the surrounding fluid. This results in a locally reduced Sh, as shown in Fig. 11 where a typical local Sherwood number Sh_θ evolution is evidenced between the front and the rear of the droplet. Under this particular configuration, Sh_θ even changes its sign at the rear for $\mu^* = 5$, meaning that the solute transfer is reversed and directed from the external fluid recirculating in the wake towards the droplet.
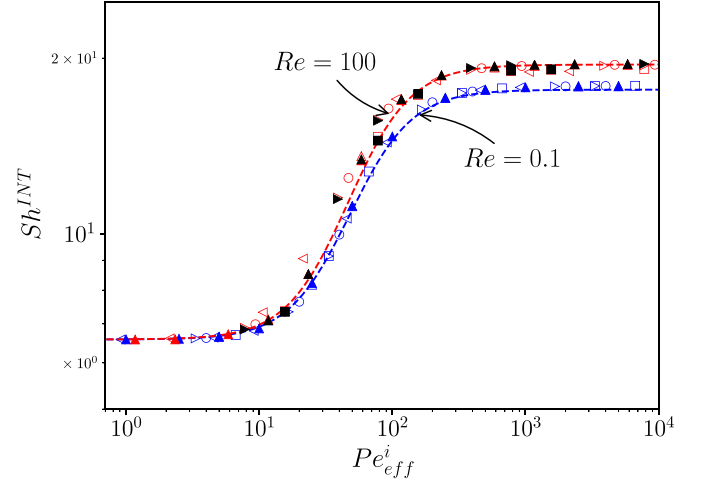
4.2.2. Asymptotic regimes

The fundamental relation of the Lewis-Whitman two-film model in conjugate transfer is based on additivity rule of the transfer resistances:

$$\frac{1}{Sh} = \frac{1}{Sh^i} + \frac{D^*k}{Sh^e} \qquad (17)$$

where Sh^i and Sh^e respectively stands for the internal Sherwood number (related to the internal resistance h^i) and the external Sherwood number (related to the external resistance h^e). This relation reflects mass flux balance at the interface, and it is always verified under the assumptions of our study (no material accumulation, no chemical reaction). It is common that Sh^i and Sh^e are approximated by the asymptotic Sherwood number characterizing the internal and the external problems, Sh^{INT} and Sh^{EXT} in Eq. (17), as these latter can be obtained from literature correlations (see Section 1 for a review). However, several authors have observed that this approximation, which can not be justified by mass balance equations, may lead to a flawed estimate of the overall conjugate mass transfer rate Sh [21].

In this section, the internal Sherwood number Sh^i (resp. the external Sherwood number Sh^e) and the Sherwood number typical of the internal regime Sh^{INT} (resp. the external regime Sh^{EXT}) are compared in limiting situations where $k\sqrt{D^*} \ll 1$ (resp. $\gg 1$), according to the criteria established by Wylock et al. [5]. Although the same hydrodynamic and physical-chemical properties were considered,

the "internal" (resp. "external") simulations leading to Sh^{INT} (resp. Sh^{EXT}) were achieved by imposing the typical conditions of this extreme regime (corresponding to uniform and constant surface concentration, as previously mentioned in Section 3). Of course, no such constraint was prevailing in the DNS simulations leading to Sh^i (or Sh^e) for which concentration distribution at the interface is free to evolve. At last, as the effect of k has been rarely studied in previous works, the $k\sqrt{D^*}$ criterion has been varied in two ways: either by fixing the value of k while decreasing (resp. increasing) that of D^*, or conversely by changing k while keeping the diffusivity ratio constant.

Internal problem As discussed in Section 1, some numerical studies have been dedicated so far to internal problems in viscous drops or bubbles where the transfer in the outer phase is not limiting. For bubbles, the resistance of the transfer resides in the gas phase for very soluble gases when the mass transfer liquid-phase resistance can be negligible. In such situations, the concentration on the interface is uniformly fixed, as e.g.: Juncu [30] for $\mu^* = 1$, Colombet et al. [9] for $\mu^* = 0.018$ (gas bubble in water), and Alexandrova et al. [14] at low Re and $0.5 \le \mu^* \le 10$. In all these studies, the solute transport equation is solved inside a viscous sphere considering steady flow. In Section 3, the simulation of internal problems has been validated in low Reynolds configurations, by comparison with available data from literature. Results have shown that the temporal evolution of the internal Sherwood number in this configuration converges to a different steady state depending on the presence or absence of internal recirculation.

The comparison between existing Sh^{INT} correlations is not trivial, as the scaling parameters are generally different: see the definitions of effective internal Péclet numbers, Pe^i_{eff}, introduced by Oliver and De Witt [35] for droplets, and by Colombet et al. [9]. Similarly to the methodology used for the drag coefficient, Eq. (16), we modified the expression proposed by Colombet et al. [9], replacing Pe^i by $Pe^i/(\mu^* + 1)$ to account for droplet viscosity. Thanks to this extension, the Colombet et al. [9] correlation Eq. (C.1) collapses all the literature data, as well as the Sh^{INT} data obtained from our simulations (Fig. 12), where an effective Péclet number Pe^i_{eff} accounting for the interfacial advection involved in the transfer is defined as:

$$Pe^i_{eff} = \left(\frac{16 + 3.315Re^{1/2} + 3Re}{16 + 3.315Re^{1/2} + Re} \right) \cdot \left(\frac{Pe^i}{\mu^* + 1} \right) \qquad (18)$$
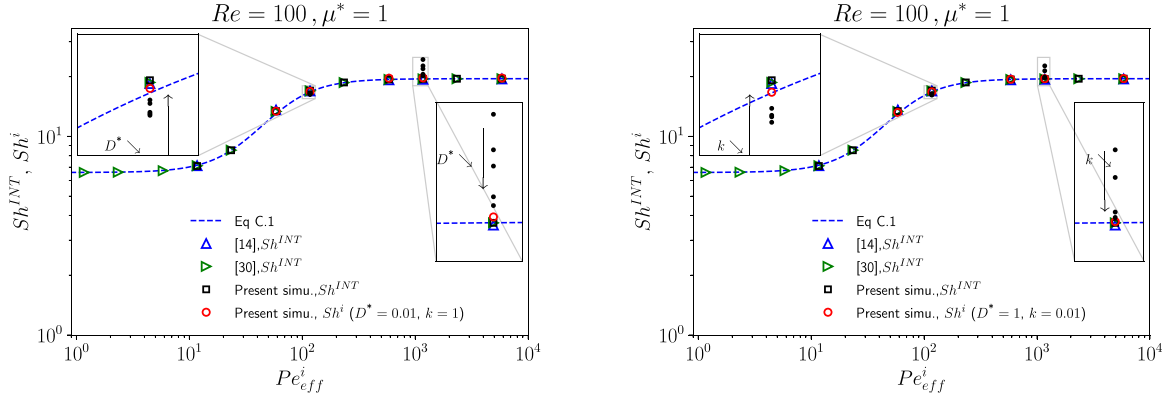
Fig. 13. Evolution of internal Sherwood number Sh^i (red circles) and comparison with the Sherwood number of the internal problem Sh^{INT} (black dots). Sh^{INT} data of Juncu [30] (green symbols) and correlation of Colombet et al. [9] (blue dash line) are reported for comparison. On the left: $k = 1$, D^* is varied. On the right: k is varied, $D^* = 1$. (For interpretation of the references to colour in this figure legend, the reader is referred to the web version of this article.)
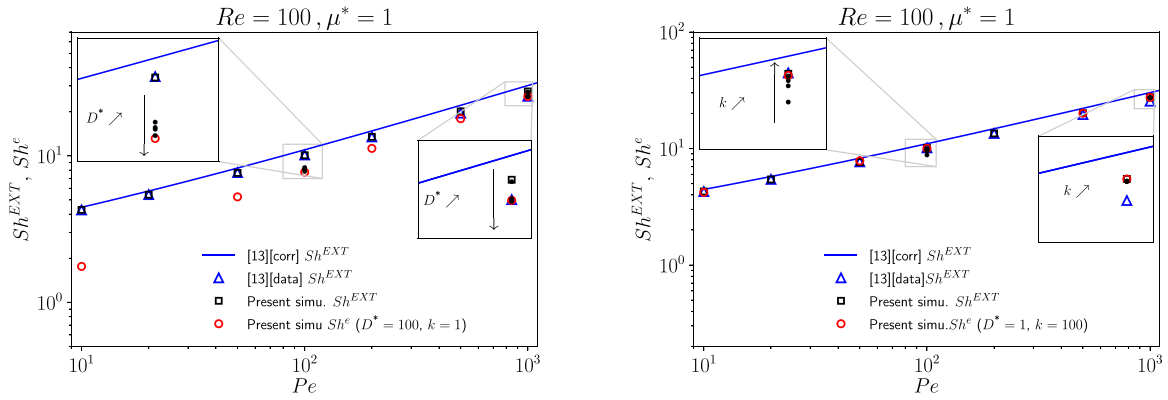
Fig. 14. Evolution of external Sherwood number Sh^e (red circles) and comparison with the Sherwood number of the external problem Sh^{EXT} (black squares). Sh^{EXT} data and correlation of Feng and Michaelides [13] (blue triangles and blue line) are reported for comparison. On the left: $k = 1$, D^* is varied. On the right: k is varied, $D^* = 1$. (For interpretation of the references to colour in this figure legend, the reader is referred to the web version of this article.)

Internal problem and internal transfer Transfer is expected to be controlled by internal features when $k\sqrt{D^*} \ll 1$. The Sherwood number of the internal problem Sh^{INT}, Eq. (C.1), and the internal Sherwood number Sh^i predicted by DNS without any assumption regarding the surface and external concentrations are compared in Fig. 13.

Discrepancy between Sh^i and Sh^{INT} is observed in conjugate transfer, as the internal resistance to mass transfer is not equal to the one of the internal problem. The discrepancy is reduced for $k = 1$ when D^* decreases (left figure), and similarly for $D^* = 1$ when k decreases (right figure). Hence, in the first case, the reduction of D^* corresponds to an increase of D^e, which was observed to homogenize the spatial distribution of the solute outside the drop, and so the interface concentration. Conversely, as mentioned above, reducing k (at fixed D^*) confines the solute inside the drop. Although the transfer is slower, this tends to homogenize the concentration inside the drop, and so the interface concentration. For high Pe^i these configurations are comparable to an internal problem. A small gap between Sh^i and Sh^{INT} is however still prevailing in configurations where $k\sqrt{D^*} \ll 1$ at small values of the Péclet number. Indeed, as illustrated by Fig. C.23 in Appendix C, the temporal evolution of Sh^i in this configuration does not converge to well established steady value, as it is the case for higher Pe^i. Despite this evolution, the average value is close to the corresponding Sh^{INT}, and a deviation of less than 4% is observed.

External problem In an external problem, the transfer resistance is mainly located outside the drop. Many correlations have been developed for the external Sherwood number Sh^{EXT} that are cited in Section 1. Aoki et al. [16] experimentally confirmed the effect of

surface active component adsorption on the mass transfer from a dissolving bubble and proposed, for fully contaminated Taylor bubbles, a correlation for the Sh^{EXT} based on the Eotvos number. Using the same experimental setup, Hori et al. [17] observed a decrease of the Sh with increasing salt concentration in the liquid phase. As no effect was observed on the rising velocity of the bubble, the decrease in the mass transfer rate was attributed to the reduction of the dissolved gas diffusivity in the liquid phase. In the case of clean and spherical droplets, the DNS values of Sh^{EXT} reveal excellent agreement with the correlation proposed by Feng and Michaelides [13] (Eq. (C.2) in Appendix C).

External problem and external transfer Transfer is expected to be controlled by external mass boundary layer when $k\sqrt{D^*} \gg 1$. The Sherwood number of the external problem Sh^{EXT}, Eq. (C.2), and the external Sherwood number Sh^e predicted by DNS (surface and external concentrations free to evolved) are compared in Fig. 14.

Larger discrepancies between Sh^e and Sh^{EXT} are observed in conjugate transfer, compared to cases for internal resistance/problem. The difference is about 10% for $Pe = 1000$ and $D^* = 100$. In order to understand the origin of this discrepancy between the steady value of Sh^e and Sh^{EXT}, the steady-state concentration at the interface was plot for $k = 1$ (see Fig. C.24). A non uniform concentration distribution is observed for $D^* = 100$, for both $Pe = 100$ and $Pe = 1000$. This is the origin of the difference with external problem for which uniform concentration is fixed at the interface. However, when k is increased (right part of Fig. 14), the gap reduces as the mass transfer is further shifted outwards by the adverse thermodynamic conditions. The deviation is less than 1% for $k = 10$.
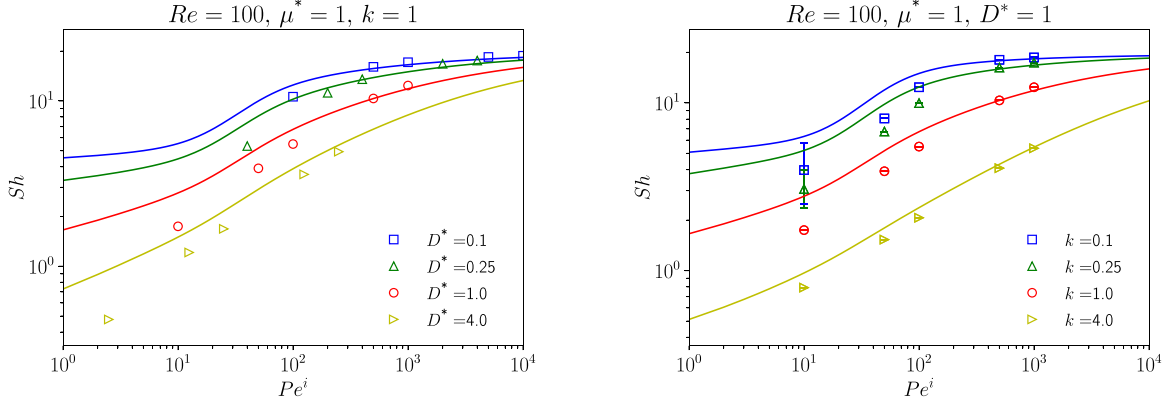
Fig. 15. Evolution of global Sherwood number *Sh* of the conjugate mass transfer problem with internal Péclet Pe^i at $Re = 100$ and for $\mu^* = 1$. Comparison of the DNS results (symbols) with Eq (19) (solid lines). The error bars represent the extreme values of *Sh* within the time interval for averaging.
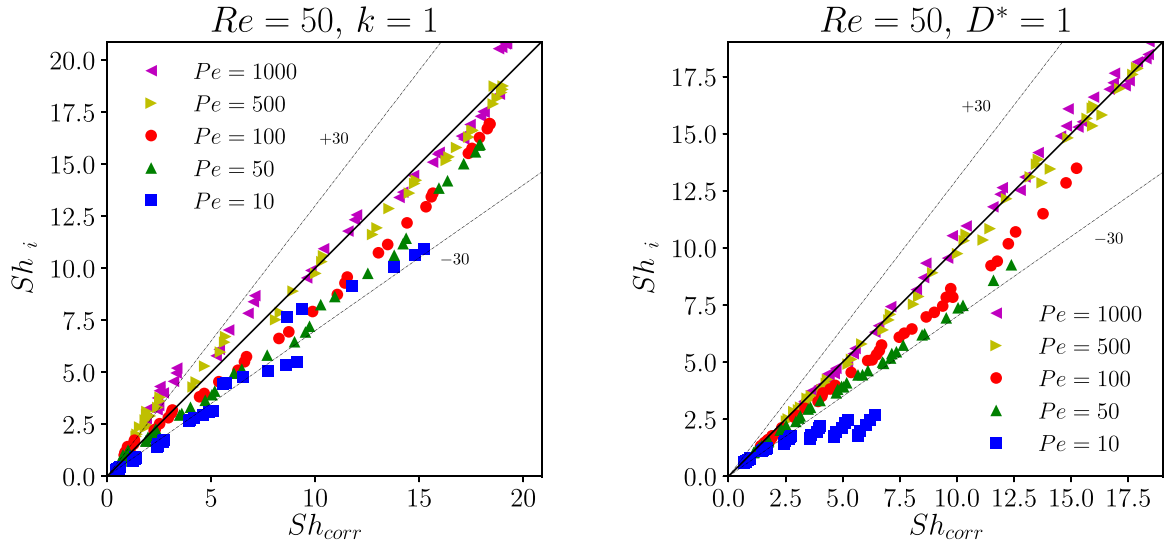
Fig. 16. Parity plot of Sherwood number. $Re = 50$, $k = 1$ (left), $D^* = 1$ (right). Sh_{corr} corresponds to Sherwood number from correlation Eq (19) and Sh_{sim} to DNS results.

4.2.3. Global transfer in a conjugate regime for Re ≤ 100

Substituting Sh^i (resp. Sh^e) with Sh^{INT} (resp. Sh^{EXT}) in Eq. 17 is not rigorously exact. Several attempts have been made to relate the global Sherwood number of a conjugate problem to the Sherwood numbers associated respectively to the internal Sh^{INT} and external Sh^{EXT} problems assuming additivity rule of transfer resistances [21], Oliver and Chung [36], Nguyen et al. [37]:

$$\frac{1}{Sh} = \frac{1}{Sh^{INT}} + \frac{D^*k}{Sh^{EXT}} \tag{19}$$

Thanks to the results of the DNS parametric study, the validity of Eq. (19) could be investigated. Correlations (C.2) and (C.1), previously introduced for the external and internal problems, are used to evaluate the global Sherwood number according to Eq. (19). Note that since Sh^{INT} and Sh^{EXT} correlations rely respectively on Pe^i and Pe, we replaced Pe by its equivalent formulation D^*Pe^i in Eq. (C.2) and used Pe^i as the reference value of the Péclet number. The evolution of the global Sherwood number *Sh* obtained from DNS simulations (conjugate problem), with Pe^i is illustrated in Fig. 15 at $Re = 100$ for $\mu^* = 1$. It is compared with the corresponding evolution of *Sh*, estimated from Eq. (19). In the left figure, the influence of D^* is assessed for $k = 1$, while the effect of k is illustrated at a constant diffusivity ratio $D^* = 1$ in the right figure.

For small values of Pe^i, the temporal evolution of *Sh* given by the DNS simulations does not converge to a well defined value when D^* (resp. k) decreases while keeping $k = 1$ (resp. $D^* = 1$). This behaviour has been already observed for the internal problem study (i.e. Appendix C). In that case, the time-average of *Sh*, between the time *Fo* at which the last oscillation is observed and the final value of *Fo* (corresponding to $\overline{C^i} \approx 10^{-4}$), is considered. The error bars in Fig. 15 represent the extreme values of *Sh* within the time interval for averaging.

The trend is consistent with previous comments. Hence, for $k = 1$ (meaning concentration continuity at the interface, which is formally equivalent to heat transfer case), the figure on the left hand side highlights the typical effects of diffusion and convection already observed at small *Re*. Similarly, as already observed the higher the value of k (*i.e.* the affinity of the solute for the liquid in the droplet), the lower the mass transfer rate (smaller *Sh*).

The accuracy of Eq. (19) decreases at small Pe^i, which is consistent with the previous comparisons of Sh^e with the corresponding values for the external regimes Sh^{EXT} due to non-uniform and unsteady surface concentration. Interestingly, the agreement between simulations and the *Sh* correlation improves as k increases. While for small values of the equilibrium constant $k \leq 1$ (when thermodynamics is adverse to the solute transfer towards the continuous phase), only high Pe^i yields good agreement between the simulations and the correlation. Moreover, for $k = 1$, good agreement is

observed only for $Pe^i > 100$, whichever value of D^*. Same conclusions were drawn for different viscosity ratios (see Appendix C).

Following the previous analysis, parity plots gathering more results of the parametric study ($0.25 \leq \mu^*$, D^*, $k \leq 5$) have been constructed (Fig. 16) For every values of Pe^i, Sh values from correlation and simulations have been represented with the same colour, independently of the values of μ^*, D^* and k. In agreement with the previous observations and discussion, the present simulations and the predictions based on additivity rule agree with 30% error for $Pe^i \geq 500$. When the Péclet decreases to 10, a significant deviation is observed (blue squares).

5. Conclusion

A detailed hydrodynamic analysis of a droplet embedded in a moderate Reynolds number flow has been carried out by DNS. The effects of the external Reynolds, and the viscosity ratio have been studied in configurations involving both internal and external flows. Using the limits of high viscosity ratio (typical of a rigid particle), and low viscosity ratio (corresponding to a bubble), a correlation of the drag coefficient has been proposed and validated up to $Re \leq 200$. Moreover, the condition under which an external circulation occurs in the wake of the drop has been obtained, and we proposed a correlation for the separation angle.

Based on this flow analysis, mass transfer simulations were performed for Reynolds numbers up to $Re = 100$ and over a wide range of physical properties. Preliminary results, at moderated Re, revealed perfect agreement between the DNS results and previous works from literature. The coupled effects of hydrodynamic and physical properties on the local and the global Sherwood numbers, and on the spatial distribution of the solute concentration have been analyzed. The possible relation with the internal/external problems has been described. *i)* Regarding internal transfer, the diffusivity ratio and partition coefficient play an equivalent role in shifting the mass transfer resistance towards the drop internal region. The internal Sherwood number Sh^i converges to the corresponding value Sh^{INT} of an internal problem when $k\sqrt{D^*} \ll 1$. *i)* For external transfer, only k plays a major role in moving the resistance towards the outer phase. The effect of D^* for high k is weak. For high diffusivity ratio, concentration at the interface is usually not uniform which results in a significant deviation between the external Sherwood number Sh^e and corresponding Sh^{EXT} for low Pe. In this case, an increase of k allows to reduce the difference between Sh^e and Sh^{EXT}.

At last, regarding the prediction of the global Sherwood number typical of a conjugate problem, the relevance of using correlations valid for the asymptotic "External" and "Internal" mass transfer regimes, in the additivity rule of transfer resistances, known as the Lewis-Whitman double film-model, was evidenced for high internal Péclet number and high partition coefficient. This common assumption is actually incorrect at low Pe, for which discrepancy larger than 30% was observed. Besides this important recommendation, it was however not possible to propose a universal correlation for the conjugate mass transfer problem. Indeed, as discussed in Section 4.2, the internal and external resistances that actually prevail on both sides of the interface can not be easily correlated in this case, due to either radial concentration gradients in the droplet, or local variations over the interface and/or outside concentration, etc.

Declaration of Competing Interest

The authors declare that they have no known competing financial interests or personal relationships that could have appeared to influence the work reported in this paper.

CRediT authorship contribution statement

Azeddine Rachih: Investigation, Software, Writing - original draft. **Dominique Legendre:** Software, Methodology, Validation, Formal analysis. **Eric Climent:** Supervision, Formal analysis, Visualization. **Sophie Charton:** Conceptualization, Visualization.

Acknowledgements

Appendix A. Complementary model description

A1. Dimensionless and discretized forms of governing equations

The dimensionless form of the Navier-Stokes Eqs. (1) and (2) in the curvilinear coordinate system $\xi_i = (\xi_1, \xi_2)$ writes in phases $\delta = (i, e)$ for internal and external fluid:

$$\frac{\partial V_j^\delta}{\partial \xi_j} = 0 \tag{A.1}$$

$$\frac{\partial V_i^\delta}{\partial t} + \frac{\partial (V_i^\delta V_j^\delta)}{\partial \xi_j} = -\frac{\partial p^\delta}{\partial \xi_i} + \frac{\partial (\tau_{ij}^\delta)}{\partial \xi_j} + H_j^i(V_j^\delta V_j^\delta - \tau_{jj}^\delta) - H_j^i(V_i^\delta V_j^\delta - \tau_{ij}^\delta) \tag{A.2}$$

The stretching factors (curvature terms) H_i^j are defined as:

$$H_i^j = \frac{1}{h_i}\frac{\partial h_i}{\partial \xi_j} \tag{A.3}$$

where h_k denotes the scale factor along the direction ξ_k, and τ_{ij}^δ represents the dimensionless viscous stress given in the considered orthogonal curvilinear coordinates by:

$$\begin{aligned}\tau_{ij}^i &= \frac{1}{Re}\left[\frac{\partial V_i^i}{\partial \xi_j} + \frac{\partial V_j^i}{\partial \xi_i} - H_i^j V_j^i - H_i^j V_i^i + 2H_i^k V_k^i \delta_{ij}\right] \\ \tau_{ij}^e &= \frac{\mu^*}{Re}\left[\frac{\partial V_i^e}{\partial \xi_j} + \frac{\partial V_j^e}{\partial \xi_i} - H_i^j V_j^e - H_i^j V_i^e + 2H_i^k V_k^e \delta_{ij}\right]\end{aligned} \tag{A.4}$$

Re is expressed relatively to the continuous (external) phase and δ_{ij} is the Kronecker delta symbol.

The solute balance equation Eq. (3) in phases δ writes:

$$\begin{aligned}\frac{\partial C^i}{\partial t} + \frac{\partial (V_j^i C^\delta)}{\partial \xi_j} &= \frac{1}{Pe}\frac{\partial^2 C^i}{\partial \xi_j \partial \xi_j} \\ \frac{\partial C^e}{\partial t} + \frac{\partial (V_j^e C^e)}{\partial \xi_j} &= \frac{D^*}{Pe}\frac{\partial^2 C^e}{\partial \xi_j \partial \xi_j}\end{aligned} \tag{A.5}$$

The dimensionless concentration of the solute in each phase δ is defined as:

$$C^\delta = \frac{C'^\delta - C_\infty'^e}{C_0'^i - C_\infty'^e} \tag{A.6}$$

The prime refers to dimensional concentration, while $C_0'^i$ stands for the droplet initial concentration (assumed uniform) and $C_\infty'^e$ for the solute concentration in the fluid flow, far from the droplet. $Pe = \frac{2U_0 R}{D^e}$ is the external Péclet number and D^* is the ratio of mass diffusivities D^i/D^e.

The interface conditions Eqs. (4) and (5) are discretized using second order differentiation (Fig. A.17) in order to express the interfacial shear:

$$\tau_{12,S}^i = \tau_{12,S}^e = \mu^* \frac{\Delta_3^i V_{1,j-2} - \Delta_2^i V_{1,j-1} + \frac{(\Delta_1^i - H_{1,S}^2)(\Delta_2^e V_{1,j} - \Delta_3^e V_{1,j+1})}{\Delta_1^e + H_{1,S}^2}}{1 + \mu^* \frac{\Delta_1^i - H_{1,S}^2}{\Delta_1^e + H_{1,S}^2}}, \tag{A.7}$$
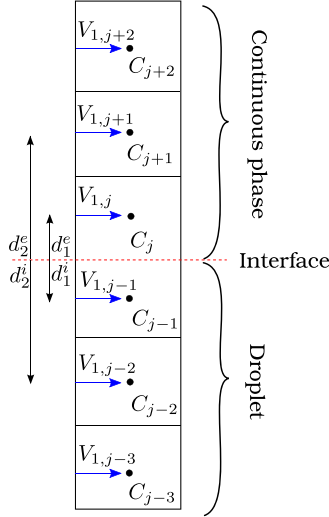
Fig. A.17. Discretization along the ξ_2 direction across the interface.

the interfacial velocity:

$$V_S^i = V_S^e = \frac{\Delta_2^e V_{1,j} - \Delta_3^e V_{1,j+1} - \tau_{12,S}^e}{\Delta_1^e + H_{1,S}^2}, \tag{A.8}$$

the interfacial concentrations:

$$C_S^e = k C_S^i = \frac{\Delta_2^e C_j - \Delta_3^e C_{j+1} + D^*(\Delta_2^i C_{j-1} - \Delta_3^i C_{j-2})}{\Delta_1^e + D^* k \Delta_1^i}, \tag{A.9}$$
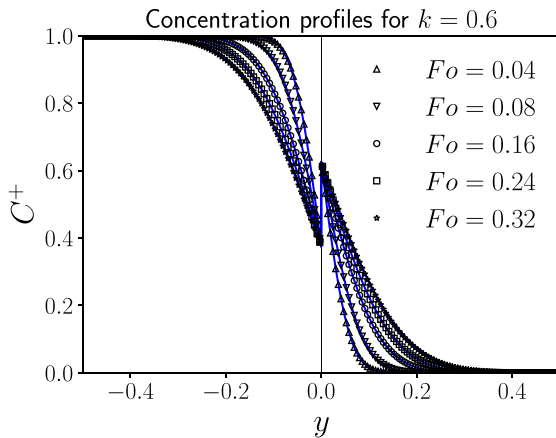
and the concentration gradients normal to the interface:

$$\left(\frac{\partial C^e}{\partial \xi_2}\right)_S = D^* \left(\frac{\partial C^i}{\partial \xi_2}\right)_S$$
$$= \frac{k \Delta_1^i (\Delta_2^e C_j - \Delta_3^e C_{j+1}) - \Delta_1^e (\Delta_2^i C_{j-1} - \Delta_3^i C_{j-2})}{k \Delta_1^i + \frac{1}{D^*} \Delta_1^e}. \tag{A.10}$$

with the curvature at the interface given by $H_{1,S}^2 = 1/R$ and the following definitions for the discretization factors as function of the nodes distances d_1^δ and d_2^δ on both side of the interface (see Fig. A.17):

$$\Delta_1^\delta = \frac{d_2^{\delta 2} - d_1^{\delta 2}}{d_1^\delta d_2^\delta (d_2^\delta - d_1^\delta)} \tag{A.11}$$

$$\Delta_2^\delta = \frac{d_2^{\delta 2}}{d_1^\delta d_2^\delta (d_2^\delta - d_1^\delta)} \tag{A.12}$$

$$\Delta_3^\delta = \frac{d_1^{\delta 2}}{d_1^\delta d_2^\delta (d_2^\delta - d_1^\delta)} \tag{A.13}$$

A2. Validation of interface boundary conditions

A2.1. 1D diffusion and thermodynamic equilibrium at a plane interface

In order to verify the implementation of the boundary conditions for the concentration, especially in the case of discontinuous concentration at the interface (thermodynamic equilibrium with k different from 1), we consider solute diffusion between two quiescent liquids. $y<0$ (resp. $y>0$) corresponds to liquid 1 with diffusion coefficient D_1 (resp, 2 with D_2). Phases are supposed to be infinite in the directions (x, z), so that the problem is 1D Cartesian. The analytical unsteady solution is given in Eq (A.14). For the numerical simulations, the following conditions were considered: $(D_1 = D_2; C_1^0 = 1; C_2^0 = 0)$. We studied the influence of the Henry coefficient k, responsible for the concentration discontinuity at the interface. The simulation results are in excellent agreement with the analytical solution (Fig. A.18). The concentration discontinuity at the interface is correctly imposed at any time in the simulation verifying $C_1 = k C_2$ at $y = 0$ and mass flux balance at the interface. The value of the concentration at the interface is not time-dependent $(C_1(y = 0) = \frac{k}{1+k}$ and $C_1(y = 0) = \frac{1}{1+k})$.

$$\begin{aligned} C_1^+ &= \left(\frac{D_2}{D_2 + k \cdot D_1}\right)\left(\frac{k \cdot C_2^0 - C_1^0}{C_2^0 - C_1^0}\right) erfc(-u_1) \\ C_2^+ &= \left(\frac{D_1}{D_2 + k \cdot D_1}\right)\left(\frac{k \cdot C_2^0 - C_1^0}{C_2^0 - C_1^0}\right) erfc(u_2) \end{aligned} \tag{A.14}$$

with

$$\begin{cases} C_1^+ &= \frac{C_1 - C_1^0}{C_2^0 - C_1^0} \\ C_2^+ &= \frac{C_2 - C_2^0}{C_1^0 - C_2^0} \\ u_1 &= \frac{y}{2\sqrt{D_1 t}} \quad for \quad y < 0 \\ u_2 &= \frac{y}{2\sqrt{D_2 t}} \quad for \quad y > 0 \end{cases} \tag{A.15}$$

A2.2. Unsteady diffusion within a stagnant spherical droplet

We consider the classical problem of unsteady solute diffusion inside a stagnant droplet ($Pe = 0$ and $Re = 0$). The concentration inside the droplet has been initialized at C_0, and the concentration at the interface is fixed at C_S (internal problem). The instantaneous radial profile of the normalized concentration $C^+ = \frac{C^i - C_0^i}{C_S - C_0^i}$ is given
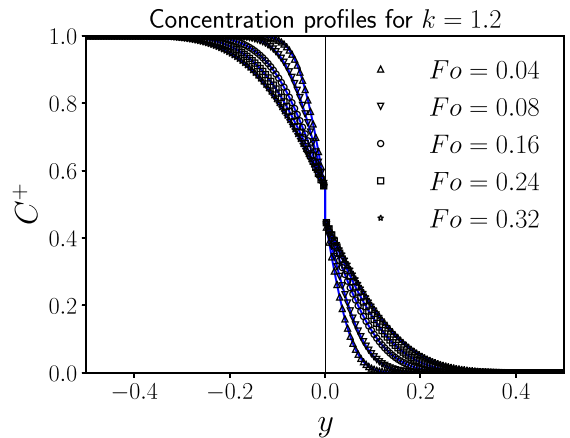

Fig. A.18. Time evolution of the concentration across the interface (symbols: simulation - blue line: analytic solution for infinite domain). (For interpretation of the references to colour in this figure legend, the reader is referred to the web version of this article.)
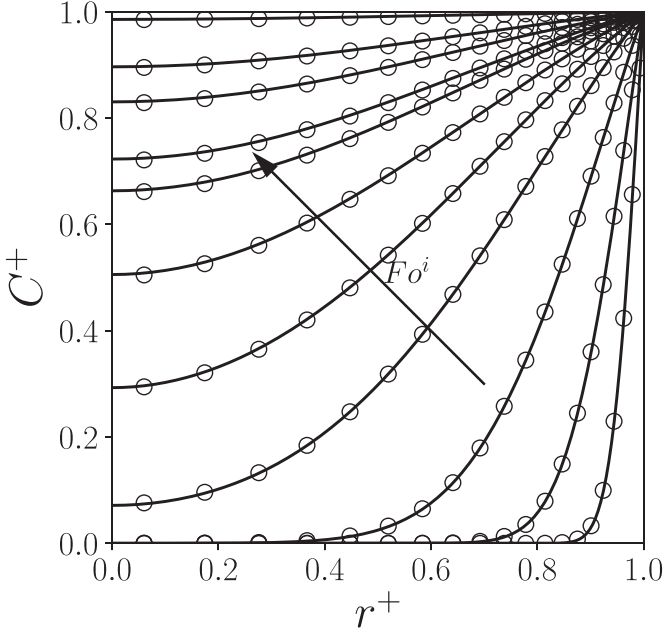
Fig. A.19. Time evolution of the concentration within a stagnant droplet.

by Newman [6] in Eq. (A.16).

$$C^+ = 1 + \frac{2}{r^+} \sum_{n=1}^{+\infty} \frac{(-1)^n}{n\pi} \exp\left(-(n\pi)^2 Fo^i\right) \sin\left(n\pi r^+\right) \qquad \text{(A.16)}$$

R has been chosen as a reference length such that $r^+ = r/R$. The Fourier number is defined by $Fo^i = \frac{D^i t}{R^2}$ with D^i the diffusion coefficient of the solute inside the droplet. The instantaneous Sherwood number is given by Eq. (A.17):

$$Sh = \frac{2\pi^2}{3} \frac{\sum_{n=1}^{+\infty} \exp\left(-(n\pi)^2 Fo^i\right)}{\sum_{n=1}^{+\infty} \frac{1}{n^2} \exp\left(-(n\pi)^2 Fo^i\right)} \qquad \text{(A.17)}$$

The Sherwood number reaches the steady state value $Sh_{Newman} = 2\pi^2/3 \approx 6.58$ in the limit of $Fo^i \longrightarrow \infty$. Radial concentration profiles from Eq (A.17) and our DNS simulation are compared in Fig. A.19 for different dimensionless times. A very good agreement is observed between our simulations (symbols) and the Newman's solution (lines). The corresponding asymptotic Sherwood number obtained by DNS is $Sh_\infty = 6.56$, which differs only by 0.2% from Newman's theoretical prediction.

Appendix B. Complementary hydrodynamic data and results

B1. Prediction of the separation angle

For intermediate to high Reynolds number flow and viscosity ratio, an external circulation may occur in the wake of the droplet. Comparing with a solid particle, the internal circulation delays both the onset of flow separation and wake formation in the external fluid for a circulating drop. The separation angle θ_d measures the angle at which the external boundary layer is detached from the spherical surface. This angle can characterize also the position at which the vorticity ω_S^e of the external phase changes its sign at the interface.

$$\omega_S^e = -\frac{\partial V_1^e}{\partial \xi_2}\bigg|_S - H_1^2 V_S^e \qquad \text{(B.1)}$$

Clift et al. [4] have shown that for a solid particle, the flow is unseparated for $0 < Re < 20$, while a steady wake region is then developed for $20 < Re < 130$. Thus, $Re = 20$ represents the onset
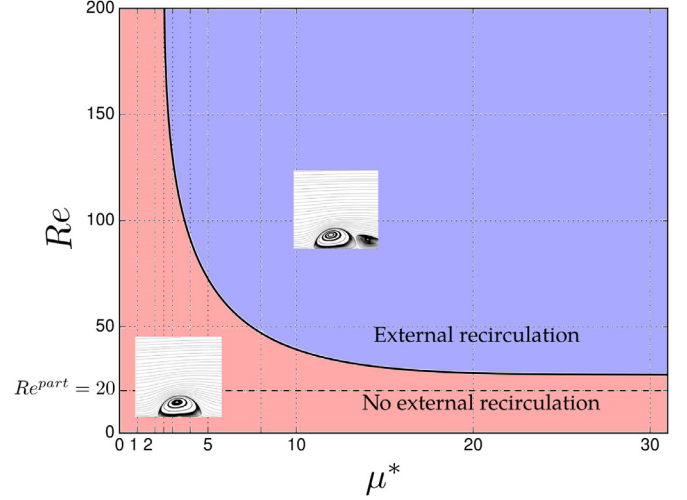

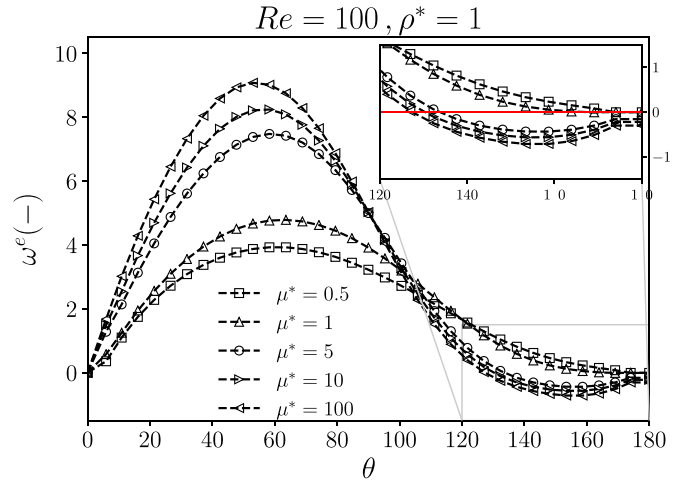**Fig. B.20.** Schematic external bifurcation diagram ($\rho^* = 1$).

Fig. B.21. Vorticity profiles along the interface ($Re = 1$, $\rho^* = 1$).

of separation for infinite viscosity ratio. The authors reported the following correlation of the separation angle which is valid for $20 < Re < 400$.

$$\theta_d = 42.5[\log(Re/20)]^{0.483} \qquad \text{(B.2)}$$

For a spherical gas bubble in liquid clear of surfactants, no separation is predicted ($\theta_d = 0$) whatever the Reynolds number [38]. This is supported by our results that for small viscosity ratio (less than $\mu^* = 0.02$), no recirculation is observed in the range of Reynold number $Re \leq 200$. Fig. B.21 shows the vorticity profiles along the interface for different configurations. We note that for a given Reynolds number (here $Re = 100$), the maximum of the interface vorticity increases with the viscosity ratio. For $\mu^* \geq 5$, the vorticity changes its sign, which proves that an external separation occurs at an angle where $\omega_S = 0$.

We can characterize the presence or the absence of the external recirculation by a schematic curve (Fig. B.20). In the pink region (*i.e.* below the curve) the external flow is unseparated, whereas an external recirculation is occurring in the blue area. As μ^* tends to higher values, the droplet behaves live a solid particle which justifies that the critical Reynolds number of separation tends towards $Re = 20$. On the oher hand, at low viscosity, the bubble-like behaviour is observed and no separation occurs.

Table B.5 reports the angles of separation for different (Re, μ^*). Some of the corresponding streamlines are highlighted in Fig. 8.

Table B.5
Separation angles in degrees.

μ^* / Re	50	100	150	200
3	no	41	46	48
5	34	46	51	55
10	37	50	55	59
15	38	51	57	61
100	40	53	60	65
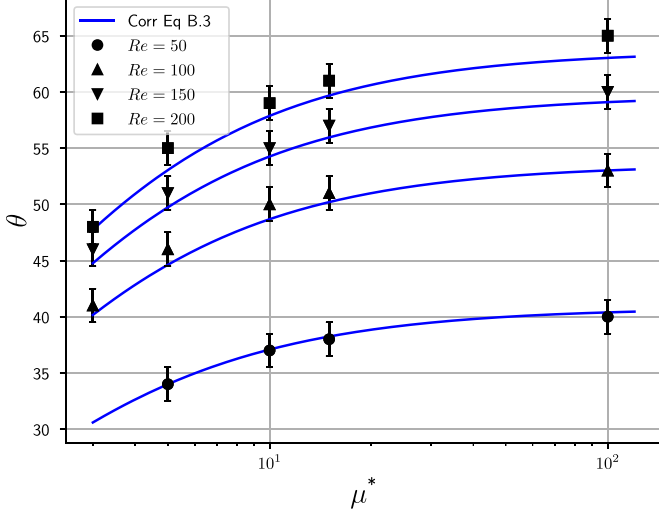
Fig. B.22. Separation angle : symbols : present simulations, blue lines : correlation Eq. (B.3). (For interpretation of the references to colour in this figure legend, the reader is referred to the web version of this article.)

In order to extend relation (B.2) to droplets, we propose the relation:

$$\theta_d = 42.5[\log(Re/20)]^{0.483} \frac{\mu^*}{1+\mu^*} \tag{B.3}$$

that gives the separation angle (relation (B.2)) in the solid sphere limit ($\mu^* \longrightarrow \infty$) and no separation ($\theta_d = 0$) in the bubble limit ($\mu^* \longrightarrow 0$).

Fig. B.22 shows the comparison between our results and the new correlation. With an error bar of $\pm 1.5°$, the correlation yields satisfactory results.

B2. Drag coefficient correlations

Correlation of Feng and Michaelides [29] for $5 < Re < 1000$ used to validated the C_D predictions:

$$C_D(Re, \mu^*) = \begin{cases} \frac{2-\mu^*}{2}C_D(Re, 0) + \frac{4\mu^*}{6+\mu^*}C_D(Re, 2) & 0 \le \mu^* \le 2 \\ \frac{4}{\mu^*+2}C_D(Re, 2) + \frac{\mu^*-2}{\mu^*+2}C_D(Re, \infty) & 2 < \mu^* \le \infty \end{cases} \tag{B.4}$$

where:

$$\begin{cases} C_D(Re, 0) = \frac{48}{Re}\left(1 - \frac{2.21}{\sqrt{Re}} + \frac{2.14}{Re}\right) \\ C_D(Re, 2) = 17.0Re^{-2/3} \\ C_D(Re, \infty) = \frac{24}{Re}\left(1 + \frac{1}{6}Re^{2/3}\right) \end{cases} \tag{B.5}$$

Correlation of Ryvkind and Ryskin [31] for $Re \le 200$:

$$C_D = \frac{1}{\mu^*+1}\left[\mu^*\left(\frac{24}{Re} + \frac{4}{Re^{1/3}}\right) + \frac{14.9}{Re^{0.78}}\right] \tag{B.6}$$

Drag coefficients of particles [33] and bubbles [32] used in correlation (16) to make Fig. 9:

$$C_D^{particle} = \frac{24}{Re}\left(1 + 0.15Re^{0.687}\right) \quad Re \le 800 \tag{B.7}$$

$$C_D^{bubble} = \frac{16}{Re}\left[1 + \left(\frac{8}{Re} + 0.5\left(1 + 3.315Re^{-0.5}\right)\right)^{-1}\right] \quad 0.1 \le Re \le 200 \tag{B.8}$$

Appendix C. Supplementary information and results on mass transfer

C1. Correlations of the Sherwood number

Correlation of the Sherwood number for the internal problem Sh^{INT} proposed by Colombet et al. [9] used in Fig. 12:

$$\frac{Sh^{INT} - Sh^{INT}(Pe^i \to 0)}{Sh^{INT}(Pe^i \to \infty) - Sh^{INT}(Pe^i \to 0)} = \frac{1}{1 + \exp\left(-1.89 \cdot (\log(Pe^i_{eff}) - 3.49)\right)} \tag{C.1}$$

Correlation of the Sherwood number for the external problem Sh^{EXT} proposed by Feng and Michaelides [13]:

$$Sh^{EXT}(\mu^*, Pe^e, Re^e)$$
$$= \begin{cases} \frac{2-\mu^*}{2}Sh^{EXT}(0, Pe, Re) + \frac{4\mu^*}{6+\mu^*}Sh^{EXT}(2, Pe, Re) & 0 \le \mu^* \le 2 \\ \frac{4}{\mu^*+2}Sh^{EXT}(2, Pe, Re) + \frac{\mu^*-2}{\mu^*+2}Sh^{EXT}(\infty, Pe, Re) & 2 \le \mu^* \le \infty \end{cases} \tag{C.2}$$

where:

$$\begin{cases} Sh^{EXT}(0, Pe, Re) = 0.651Pe^{1/2}\left(1.032 + \frac{0.61Re}{Re+21}\right) + \left(1.6 - \frac{0.61Re}{Re+21}\right) \\ Sh^{EXT}(\infty, Pe, Re) = 0.852Pe^{1/3}\left(1 + 0.233Re^{0.287}\right) + 1.3 - 0.182Re^{0.355} \\ Sh^{EXT}(2, Pe, Re) = 0.64Pe^{0.43}\left(1 + 0.233Re^{0.287}\right) + 1.41 - 0.15Re^{0.287} \end{cases} \tag{C.3}$$

C2. Supplementary results

Fig. C.23 provides illustration of the long-time transient in the internal mass transfer rate and its deviation from the internal problem case. The non-convergence of Sh^i in this moderate Pe^i case ($Pe^i = 100$) is more pronounced with lower D^*, as highlighted by the inset in the figure.
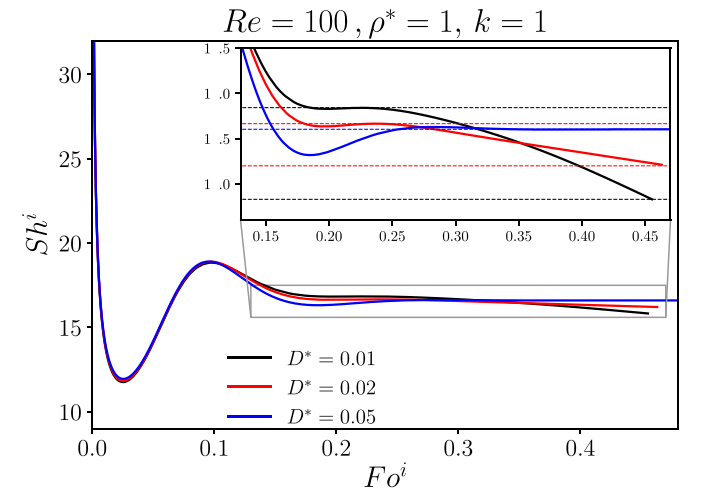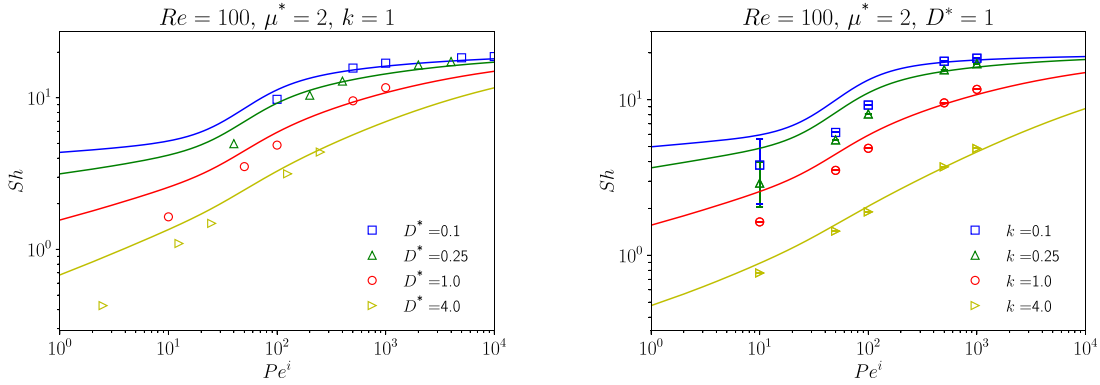

Fig. C.23. Time evolution of internal Sherwood number Sh^i with internal dimensionless time Fo^i for small D^*: $Re = 100$, $\mu^* = 1$, $k = 1$ - $Pe^i = 100$.
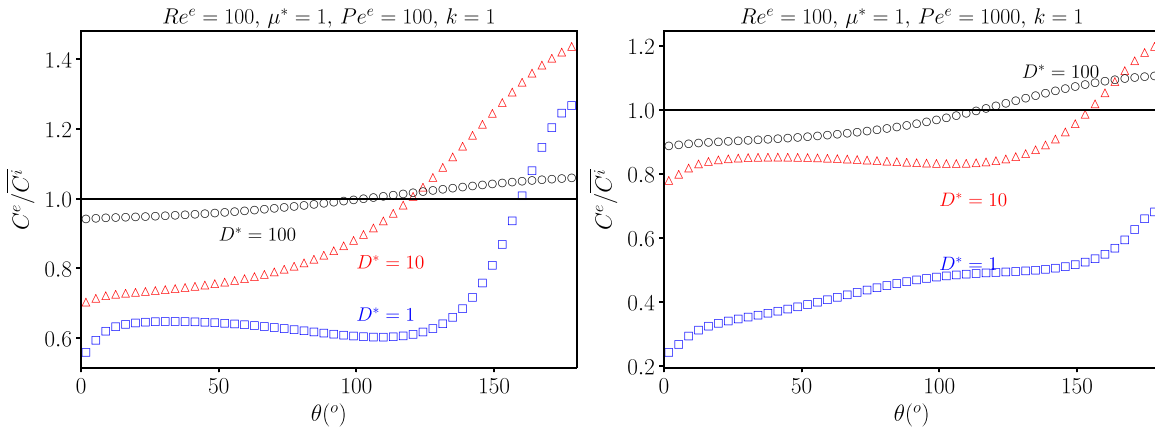
Fig. C.24. Steady profile of normalized concentration at the interface $C_s^e/\overline{C^i}$: $Re = 100$, $\mu^* = 1$, $k = 1$ - $Pe = 100$ (left), $Pe = 1000$ (right).

Fig. C.25. Evolution of global Sherwood number Sh of the conjugate mass transfer problem with internal Péclet Pe^i at $Re = 100$ and for $\mu^* = 2$. Continuous lines: Eq. (19), symbols: DNS results. The error bars represent the extreme values of Sh within the time interval for averaging.
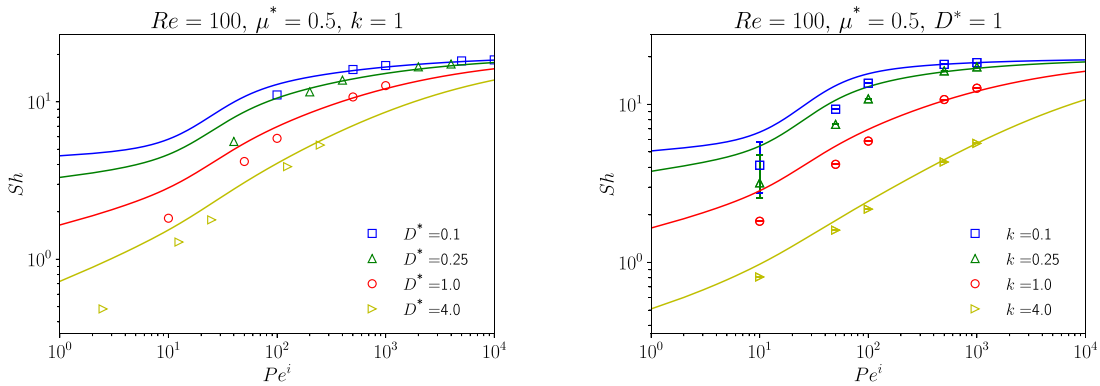
Fig. C.26. Evolution of global Sherwood number Sh of the conjugate mass transfer problem with internal Péclet Pe^i at $Re = 100$ and for $\mu^* = 0.5$. Continuous lines: Eq. (19), symbols: DNS results. The error bars represent the extreme values of Sh within the time interval for averaging.

Fig. C.24 highlights the non-uniform surface distribution of the solute concentration achieved at steady-state, which explains the discrepancies between Sh^{EXT} and Sh^e in Fig. 14.

Complementing Fig. 15 (for $\mu^* = 1$), Figs. C.25 and C.26 highlight the good agreement of the proposed correlation at high Pe and/or high k values, in the case of $\mu^* = 2$ and $\mu^* = 0.5$, respectively.

References

[1] M. Wegener, N. Paul, M. Kraume, Fluid dynamics and mass transfer at single droplets in liquid/liquid systems, Int. J. Heat Mass Transf. 71 (2014) 475–495.

[2] G. Juncu, Unsteady heat and/or mass transfer from a fluid sphere in creeping flow, Int. J. Heat Mass Transf. 44 (12) (2001) 2239–2246.

[3] G. Juncu, Unsteady ternary mass transfer from a sphere in creeping flow, Int. J. Therm. Sci. 44 (3) (2005) 255–266.

[4] R. Clift, J. Grace, M. Weber, Bubbles, Drops, and Particles, Academic Press Inc., 1978.

[5] C. Wylock, P. Colinet, B. Haut, Gas absorption into a spherical liquid droplet: numerical and theoretical study, Chem. Eng. J. 207 (2012) 851–864.

[6] A.B. Newman, The drying of porous solids: diffusion and surface emission equations, AIChE Trans. 27 (1931) 203–220.

[7] R. Kronig, J. Brink, On the theory of extraction from falling droplets, Appl. Sci. Res. 2 (1) (1951) 142.

[8] A. Brignell, Solute extraction from an internally circulating spherical liquid drop, Int. J. Heat Mass Transf. 18 (1) (1975) 61–68.

[9] D. Colombet, D. Legendre, A. Cockx, P. Guiraud, Mass or heat transfer inside a spherical gas bubble at low to moderate Reynolds number, Int. J. Heat Mass Transf. 67 (2013) 1096–1105.

[10] Z. Feng, E.E. Michaelides, Mass and heat transfer from fluid spheres at low Reynolds numbers, Powder Technol. 1123 (2000) 63–69.

[11] B. Abramzon, G. Fishbein, Some problems of convective diffusion to a spherical particle with $Pe \leq 1000$, J. Eng. Phys. 32 (6) (1977) 682–686.

[12] B. Abramzon, C. Elata, Unsteady heat transfer from a single sphere in stokes flow, Int. J. Heat Mass Transf. 27 (5) (1984) 687–695.

[13] Z. Feng, E. Michaelides, Heat and mass transfer coefficients of viscous spheres, Int. J. Heat Mass Transf. 44 (23) (2001) 4445–4454.

[14] S. Alexandrova, M. Karsheva, A. Saboni, C. Gourdon, Effect of the viscosity ratio on the mass transfer into a spherical drop in liquid-liquid dispersions, J. Chem. Technol. Metall. 49 (5) (2014) 429–434.

[15] A. Saboni, S. Alexandrova, M. Karsheva, C. Gourdon, Mass transfer from a contaminated fluid sphere, AlChE J. 57 (7) (2011) 1684–1692.

[16] J. Aoki, Y. Hori, K. Hayashi, S. Hosokawa, A. Tomiyama, Mass transfer from single carbon dioxide bubbles in alcohol aqueous solutions in vertical pipes, Int. J. Heat Mass Transf. 108 (B) (2017) 1991–2001.

[17] Y. Hori, K. Hayashi, S. Hosokawa, A. Tomiyama, Mass transfer from single carbon-dioxide bubbles in electrolyte aqueous solutions in vertical pipes, 115, Part A, 663–671, 2017, Int. J. Heat Mass Transf. 115 (A) (2017) 663–671.

[18] A. Kumar, S. Hartland, Correlations for prediction of mass transfer coefficients in single drop systems and liquid–liquid extraction columns, Chem. Eng. Res. Des. 77 (5) (1999) 372–384.

[19] E. Ruckenstein, Mass transfer between a single drop and a continuous phase, Int. J. Heat Mass Transf. 10 (12) (1967) 1785–1792.

[20] D. Oliver, J. Chung, Conjugate unsteady heat transfer from a spherical droplet at low Reynolds numbers, Int. J. Heat Mass 29 (6) (1986) 879–887.

[21] L.S. Kleinman, X. Reed, Unsteady conjugate mass transfer between a single droplet and an ambient flow with external chemical reaction, Ind. Eng. Chem. Res. 35 (9) (1996) 2875–2888.

[22] A. Paschedag, W. Piarah, M. Kraume, Sensitivity study for the mass transfer at a single droplet, Int. J. Heat Mass Transf. 48 (16) (2005) 3402–3410.

[23] J. Magnaudet, M. Rivero, J. Fabre, Accelerated flows past a rigid sphere or a spherical bubble. Part 1. Steady straining flow, J. Fluid Mech. 284 (1995) 97–135.

[24] D. Legendre, J. Magnaudet, The lift force on a spherical body in a viscous linear shear flow, J. Fluid Mech. 368 (1998) 81–126.

[25] D. Legendre, J. Magnaudet, G. Mougin, Hydrodynamic interactions between two spherical bubbles rising side by side in a viscous liquid, J. Fluid Mech. 497 (2003) 133–166.

[26] A. Merle, D. Legendre, J. Magnaudet, Forces on a high-re spherical bubble in a turbulent flow, J. Fluid Mech. 532 (2005) 53–62.

[27] B. Figueroa, D. Legendre, Mass or heat transfer from spheroidal gas bubbles rising through a stationary liquid, Chem. Eng. Sci. 65 (2010) 6296–6309.

[28] Y. Hallez, D. Legendre, Interaction between two spherical bubbles rising in a viscous liquid, J. Fluid Mech. 673 (2011) 406–431.

[29] Z. Feng, E.E. Michaelides, Drag coefficients of viscous spheres at intermediate and high Reynolds numbers, J. Fluids Eng. 123 (4) (2001) 841–849.

[30] G. Juncu, A numerical study of the unsteady heat/mass transfer inside a circulating sphere, Int. J. Heat Mass Transf. 53 (15–16) (2010) 3006–3012.

[31] V. Ryvkind, G. Ryskin, Flow structure in motion of a spherical drop in a fluid medium at intermediate Reynolds number, Fluid Dyn. 11 (5) (1976).

[32] R. Mei, J.F. Klausner, C.J. Lawrence, A note on the history force on a spherical bubble at finite Reynolds number, Phys. Fluids 6 (1) (1994) 418–420.

[33] L. Schiller, A.Z. Nauman, A drag coefficient correlation, Ver. Deut. Ing. Zeitung 77 (1933) 318–321.

[34] D. Legendre, A. Rachih, C. Souilliez, S. Charton, E. Climent, The Basset-Boussinesq history force of a fluid sphere, Phys. Rev. Fluids 4 (2019) 073603.

[35] D. Oliver, K. De Witt, Heat transfer in bubbles and droplets at moderate Reynolds numbers: interior problem, in: National Heat Transfer Conference, Portland, OR (United States), 1995.

[36] D. Oliver, J. Chung, Unsteady conjugate heat transfer from a translating fluid sphere at moderate Reynolds numbers, Int. J. Heat Mass Transf. 33 (3) (1990) 401–408.

[37] H.D. Nguyen, S. Paik, J.N. Chung, Unsteady conjugate heat transfer associated with a translating spherical droplet: a direct numerical simulation, Numer. Heat Transf. Part A 24 (2) (1993) 161–180.

[38] A. Blanco, J. Magnaudet, The structure of the axisymmetric high-Reynolds number flow around an ellipsoidal bubble of fixed shape, Phys Fluids 7 (1995) 1265.